Influence of future anthropogenic emissions on climate, natural emissions, and air quality

Mark Z. Jacobson[1] and David G. Streets[2]

[1] This study examines the effects of future anthropogenic emissions on climate, and the resulting feedback to natural emissions and air quality. Speciated sector- and region-specific 2030 emission factors were developed to produce gas and particle emission inventories that followed Special Report on Emission Scenarios (SRES) A1B and B1 emission trajectories. Current and future climate model simulations were run, in which anthropogenic emission changes affected climate, which fed back to natural emissions from lightning (NO, NO_2, $HONO$, HNO_3, N_2O, H_2O_2, HO_2, CO), soils (dust, bacteria, NO, N_2O, H_2, CH_4, H_2S, DMS, OCS, CS_2), the ocean (bacteria, sea spray, DMS, N_2O, H_2, CH_4), vegetation (pollen, spores, isoprene, monoterpenes, methanol, other VOCs), and photosynthesis/respiration. New methods were derived to calculate lightning flash rates as a function of size-resolved collisions and other physical principles and pollen, spore, and bacteria emissions. Although the B1 scenario was "cleaner" than the A1B scenario, global warming increased more in the B1 scenario because much A1B warming was masked by additional reflective aerosol particles. Thus neither scenario is entirely beneficial from a climate and health perspective, and the best control measure is to reduce warming gases and warming/cooling particles together. Lightning emissions declined by $\sim$3% in the B1 scenario and $\sim$12% in the A1B scenario as the number of ice crystals, thus charge-separating bounceoffs, decreased. Net primary production increased by $\sim$2% in both scenarios. Emissions of isoprene and monoterpenes increased by $\sim$1% in the A1B scenario and 4–5% in the B1 scenario. Near-surface ozone increased by $\sim$14% in the A1B scenario and $\sim$4% in the B1 scenario, reducing ambient isoprene in the latter case. Gases from soils increased in both scenarios due to higher temperatures. Near-surface $PM_{2.5}$ mass increased by $\sim$2% in the A1B scenario and decreased by $\sim$2% in the B1 scenario. The resulting 1.4% higher aerosol optical depths (AODs) in the A1B scenario decreased ocean wind speeds and thus ocean sea spray and bacteria emissions; $\sim$5% lower AODs in the B1 scenario had the opposite effect.

1. Introduction

[2] This study examines the effects of future anthropogenic emission changes on natural emissions and the resulting effects on climate and air quality. Several global studies have examined the feedback of anthropogenic emissions to natural emissions of isoprene, monoterpenes, other VOCs, soil dust, and/or lightning NO_x [*IPCC*, 2001; *Sanderson et al.*, 2003; *Stevenson et al.*, 2005; *Unger et al.*, 2006; *Liao et al.*, 2006]. Studies have also examined the effects of climate change on ozone or methane [e.g., *Hameed and Cess*, 1983; *Thompson et al.*, 1989; *Fuglestvedt et al.*, 1995; *Brasseur et al.*, 1998, 2006; *Johnson et al.*, 1999, 2001; *Stevenson et al.*, 2000, 2005; *Grewe et al.*, 2001; *Zeng and Pyle*, 2003; *Murazaki and Hess*, 2006; *Unger et al.*, 2006] and on ozone and aerosol particles [*Liao et al.*, 2006; *Unger et al.*, 2006; *Jacobson*, 2008]. Sensitivity studies have examined the temperature-dependence of gas photochemistry [*Sillman and Samson*, 1995; *Zhang et al.*, 1998; *Johnson et al.*, 1999] and of regional gas and particle pollution [*Aw and Kleeman*, 2003; *Steiner et al.*, 2006].

[3] Here new 2030 emission factors are developed. The resulting emission inventories are used to examine the effects of climate change on natural emissions and the resulting combined effect on air quality and climate. New numerical treatments of lightning-NO_x and pollen, spore, and bacteria emissions are derived. Changes in natural emissions and ambient concentrations of pollutants due to climate change are analyzed.

2. Description of the Model

[4] The model used was GATOR-GCMOM, a global-through-urban Gas, Aerosol, Transport, Radiation, General

[1] Department of Civil and Environmental Engineering, Stanford University, Stanford, California, USA.
[2] Decision and Information Sciences Division, Argonne National Laboratory, Argonne, Illinois, USA.

Circulation, Mesoscale, and Ocean Model. Individual algorithms have been tested against analytical or exact numerical solutions in several studies. Results from the model as a whole have been compared with paired-in-time-and-space (instantaneous, location specific) surface and/or aircraft spiral data [*Jacobson*, 1997, 2001a, 2001b; *Jacobson et al.*, 2007] and with monthly and annual data on the global scale [*Jacobson*, 2002b, 2004, 2005a]. Additional comparisons are shown here. Simulations were run on a $4°S−N \times 5°W−E$ global domain with 47 layers up to 0.22 hPa ($\approx$60 km), including 33 in the troposphere (six in the bottom 1 km). The model treated time-dependent dynamical, gas, aerosol, cloud, radiative, ocean, and land surface processes. Treatments of these processes are described in detail by *Jacobson et al.* [2007] and *Jacobson* [2006]. Only a few are described here.

[5] Gas photochemistry was solved among 128 gases and 282 kinetic reactions, and 52 photolysis reactions with SMVGEAR II. Aerosol processes were treated over two size distributions, each with 14 size bins (0.002 to 50 μm in diameter), and three hydrometeor distributions, each with 30 size bins. Particle number concentration and mole concentrations of several chemicals were predicted in each aerosol and hydrometeor size bin of each distribution (Table 1). Aerosol processes included emissions, binary and ternary homogeneous nucleation, condensation, dissolution, internal particle chemical equilibrium, aerosol-aerosol coagulation, aerosol-hydrometeor coagulation, sedimentation, dry deposition, and transport. Size- and composition-resolved aerosol-cloud interactions and aerosol/cloud microphysics were treated predominantly as described by *Jacobson* [2002a, 2003, 2004, 2006] and *Jacobson et al.* [2007].

[6] Radiative processes included UV, visible, solar-IR, and thermal-IR interactions with gases, size/composition-resolved aerosols, and size/composition-resolved hydrometeor particles. Aerosols fed back to meteorology through their effects on radiation, clouds, the relative humidity, and pressure. For example, equilibrium aerosol uptake of liquid water by hydration, which was calculated iteratively in each size bin following nonequilibrium growth, modified the absolute humidity and temperature due to latent heat exchange, affecting the relative humidity, thus the rate of water uptake. Similarly, since precipitation and evaporation changed the amount of water vapor, which was a component of air pressure, changes in aerosols affected air pressure by changing precipitation.

[7] The model predicted subgrid temperature and soil moisture over land [*Jacobson*, 2001a, 2001b], ocean mixed-layer depths, velocities, temperatures, energy transport, and mass transport in time with a two-dimensional potential enstrophy, energy, and vorticity conserving scheme [*Ketefian and Jacobson*, 2009]. Nine layers existed below each ocean mixed-layer grid cell in which energy and chemical diffusion from the mixed layer to the deep ocean and ocean chemistry were solved [*Jacobson*, 2005c]. As such, climate responses accounted for ocean feedbacks.

3. Emissions

[8] At least two methods have been used to calculate the effect of emission changes on future air quality and climate.

One is to simulate climate from an initial to future time assuming time-varying emissions estimated year to year. The second is to take the difference between a future and initial equilibrium climate, where each is determined from a different emission inventory (thus inventories for only two years are needed). Recent studies of the effects of future anthropogenic emissions on natural emissions have used the second approach [*Liao et al.*, 2006; *Unger et al.*, 2006]. Because of the computer time required, the equilibrium (second) method was chosen here as well. This method required the development of initial (present day) and future (2030) emission inventories.

3.1. Present-Day Emissions

[9] Near-present global ($1° \times 1°$ resolution) monthly emissions of NO_x, N_2O, CO, CO_2, SO_2, CH_4, and speciated organic gases were obtained from data by *Olivier et al.* [1996]. Data were for 1995, except that fractional speciation of organic gases, applied to 1995 emissions, were for 1990 since the 1995 inventory was not speciated. NH_3 emissions were by *Bouwman et al.* [1997]. Table 2 shows the global emissions from this inventory.

[10] Table 3 summarizes the baseline black carbon (BC), primary organic carbon (POC), and sulfate emissions from aircraft, shipping, other fossil fuels, biofuels, and biomass burning used and the method of determining such emissions. Emission rates of particle components K^+, Na^+, Ca^{2+}, Mg^{2+}, NH_4^+, Cl^-, SO_4^{2-}, and NO_3^-, and gases H_2, H_2O, NO, NO_2, N_2O, NH_3, SO_2, CO, CO_2, CH_4, CH_3OH, CH_3Cl, CH_3Br, C_2H_4, C_2H_6, C_3H_6, C_3H_8, HCHO, HCOOH, CH_3COOH, CH_3CHO, CH_3COCH_3, C_4H_6, C_5H_8, C_6H_6, C_6H_5CHO, $C_6H_5CH_3$, $C_6H_4CH_3CH_3$, and CH_3SCH_3 from biomass and biofuel burning were obtained by multiplying BC biofuel or biomass emission rates by the ratio of a mean biofuel or biomass emission factor for each component to that of BC by *Andreae and Merlet* [2001].

3.2. Gases From Lightning Hot Flashes and Corona Discharge

[11] Table 4 summarizes the naturally emitted gas and aerosol components treated here and the climate-sensitive variables that affected them. Lightning formed in the model under the assumption of rebound charging [*Pruppacher and Klett*, 1997], calculated by considering bounceoffs following size-resolved ice crystal−ice crystal, graupel-graupel, ice crystal−graupel, ice crystal−liquid, graupel-liquid, and liquid-liquid collisions. The resulting change in electric field strength triggered intracloud and cloud-to-ground lightning. Lightning produces primarily NO but also small amounts of NO_2, CO, HONO, HNO_3, H_2O_2, and HO_2 by channel heating and small amounts of N_2O by corona discharge [e.g., *Bhetanabhotla et al.*, 1985]. Corona discharge produces negligible NO relative to channel heating [*Coppens et al.*, 1997].

[12] The number of NO molecules produced per cubic centimeter of air per second in a cloud during channel heating was calculated as

$$E_{NO} = \frac{E_l F_{NO}}{A_{cell}} \frac{dF_r}{dt} \tag{1}$$

where E_l is the number of joules per lightning flash, F_{NO} is the number of NO molecules produced per joule of energy

Table 1. Aerosol and Hydrometeor Size Distributions Treated in the Model and the Parameters (Number Concentration and Chemical Mole Concentrations) Present in Each Size Bin of Each Size Distribution[a]

Aerosol Emitted Fossil Fuel Soot (EFFS)	Aerosol Internally Mixed (IM)	Cloud/ Precipitation Liquid	Cloud/ Precipitation Ice	Cloud/ Precipitation Graupel
number	number	number	number	number
BC	BC	BC	BC	BC
POM	POM	POM	POM	POM
SOM	SOM	SOM	SOM	SOM
$H_2O(l)$-hydrated	$H_2O(aq)$-hydrated	$H_2O(aq)$-hydrated	$H_2O(aq)$-hydrated	$H_2O(aq)$-hydrated
$H_2SO_4(aq)$	$H_2SO_4(aq)$	$H_2SO_4(aq)$	$H_2SO_4(aq)$	$H_2SO_4(aq)$
HSO_4^-	HSO_4^-	HSO_4^-	HSO_4^-	HSO_4^-
SO_4^{2-}	SO_4^{2-}	SO_4^{2-}	SO_4^{2-}	SO_4^{2-}
NO_3^-	NO_3^-	NO_3^-	NO_3^-	NO_3^-
Cl^-	Cl^-	Cl^-	Cl^-	Cl^-
H^+	H^+	H^+	H^+	H^+
NH_4^+	NH_4^+	NH_4^+	NH_4^+	NH_4^+
$NH_4NO_3(s)$	$NH_4NO_3(s)$	$NH_4NO_3(s)$	$NH_4NO_3(s)$	$NH_4NO_3(s)$
$(NH4)_2SO_4(s)$	$(NH4)_2SO_4(s)$	$(NH4)_2SO_4(s)$	$(NH4)_2SO_4(s)$	$(NH4)_2SO_4(s)$
	$Na^+ (K^+, Mg^{2+}, Ca^{2+})$	$Na^+ (K^+, Mg^{2+}, Ca^{2+})$	$Na^+ (K^+, Mg^{2+}, Ca^{2+})$	$Na^+ (K^+, Mg^{2+}, Ca^{2+})$
	soil dust	soil dust	soil dust	soil dust
	pollen/spores/bacteria	pollen/spores/bacteria	pollen/spores/bacteria	pollen/spores/bacteria
		$H_2O(aq)$-condensed	$H_2O(s)$	$H_2O(s)$

[a]POM, primary organic matter; SOM, secondary organic matter; $H_2O(aq)$-hydrated, liquid water hydrated onto dissolved ions and undissociated molecules in solution; $H_2O(aq)$-condensed, water that condensed to form liquid hydrometeors. Condensed and hydrated water existed in the same particles so that, if condensed water evaporated, the core material, including its hydrated water, remained. $H_2O(s)$ was either water that froze or deposited from the gas phase as ice. The emitted species in the fossil fuel soot distribution included BC, POM, $H_2SO_4(aq)$, HSO_4^-, and SO_4^{2-}. The remaining species were formed by gas-to-particle conversion or crystallization. Sea spray, soildust, biomass burning, biofuel burning, and other particles were emitted into the internally mixed distribution. Emitted species in sea spray included H_2O, Na^+, K^+, Mg^{2+}, Ca^{2+}, Cl^-, NO_3^-, $H_2SO_4(aq)$, HSO_4^-, and SO_4^{2-}. Those in biomass burning included the same plus BC and POM. In both cases, K^+, Mg^{2+}, and Ca^{2+} were treated as equivalent Na^+. Soildust was generic. Homogenously nucleated species (H_2O, $H_2SO_4(aq)$, HSO_4^-, SO_4^{2-}. NH_4^+) entered the internally mixed distribution. Condensing gases on all distributions included H_2SO_4 and SOM. Dissolving gases on all distributions included HNO_3, HCl, and NH_3. The liquid water content and H^+ in each bin were determined as a function of relative humidity and ion composition from equilibrium calculations. All distributions were affected by self-coagulation loss to larger sizes and heterocoagulation loss to other distributions (except the graupel distribution, which had no heterocoagulation loss).

Table 2. Speciated Baseline and Future Emissions Used Here for Inorganic and Organic Gases From Anthropogenic Sources[a]

Species	Baseline (Tg/a)	(2) 2030 A1B (Tg/a)	(3) 2030 B1 (tons/a)
Carbon monoxide	313 (1.70)	450 (1.83)	257 (1.45)
Carbon dioxide	23,800 (518)	59,172 (554)	41,338 (439)
Nitric oxide	46.1 (1.02)	83.5 (1.67)	41.6 (0.86)
Nitrogen dioxide	7.85 (0.22)	14.2 (0.24)	7.09 (0.19)
Nitrous acid	0.647 (0.017)	1.17 (0.018)	0.584 (0.014)
Nitrous oxide	11.1 (0.017)	11.1 (0.018)	9.78 (0.014)
Sulfur dioxide	132 (0.063)	169 (0.066)	92.06 (0.058)
Sulfur trioxide	5.16 (0.0025)	6.62 (0.0026)	3.60 (0.0023)
Sulfuric acid	2.11 (0.001)	2.70 (0.0011)	1.47 (0.0009)
Ammonia	58.2	58.5	58.6
Molecular hydrogen	8.91 (0.048)	12.8 (0.052)	7.33 (0.041)
Organic gases			
Methane	276	315	284
Paraffin bond group	52.7	159	129
Ethene	4.37	10.2	7.77
Olefin bond group	4.85	9.93	7.94
Methanol	4.50	10.4	7.91
Formaldehyde	0.98	2.85	2.09
Higher aldehydes	2.87	7.05	5.25
Benzene	2.51	5.84	4.49
Toluene bond group	4.63	7.76	6.88
Xylene bond group	6.46	10.0	9.21
Total organic gas	360 (0.29)	538 (0.32)	464 (0.25)

[a]Values in parentheses are aircraft emissions derived as in Table 3 for BC and POC. The remaining values are land- and ocean-based emissions [*Olivier et al.*, 1996]. The 2030 projections were obtained by applying the future emission factors developed here to the gridded baseline emission data.

Table 3. Fine-Particle Global Emission Rates (Tg C/a) of Black Carbon (BC) and Primary Organic Carbon (POC) for the Baseline, A1B, and B1 Scenarios[a]

	(a) Aircraft	(b) Shipping	(c) All Other Fossil Fuel	(d) Total Fossil Fuel (a + b + c)	(e) Biofuel	(f) Biomass Burning	(g) Total (d + e + f)
BC Base	0.0062	0.147	3.029	3.182	1.634	2.806	7.622
BC A1B	0.0062	0.155	5.616	5.777	0.808	2.806	9.391
BC B1	0.0062	0.135	3.273	3.414	0.668	2.806	6.888
POC Base	0.0062	0.047	2.371	2.424	6.490	24.12	33.03
POC A1B	0.0062	0.050	3.911	3.967	3.290	24.12	31.37
POC B1	0.0062	0.044	2.268	2.318	2.725	24.12	29.16

[a]Fine BC and POC emissions from aircraft were obtained by applying emission factors of 0.038 g BC/kg fuel [*Petzold et al.*, 1999] to the fuel use data from *Sutkus et al.* [2001] and assuming a POC/BC emission ratio of 1:1. Those from shipping were estimated by dividing the gridded monthly sulfur shipping emission rate from *Corbett et al.* [1999], which totaled 4.24 Tg S/a by 29.5 g S/kg fuel [*Corbett and Koehler*, 2003, Table 1, for 1999 data] and multiplying the result by 1.02 g BC/kg fuel for shipping [*Bond et al.*, 2004]. That for POC was obtained in the same manner, but by multiplying the result by 0.33 g POC C/kg fuel [*Bond et al.*, 2004]. Fine BC and POC for all other fossil fuel sources globally were obtained from *Bond et al.* [2004] after subtracting out shipping emissions. The totals from *Bond et al.* [2004] before subtracting out such emissions were 3.040 Tg BC C/a and 2.408 Tg POC C/a. Fine biofuel burning BC and POC emissions were obtained from *Bond et al.* [2004]. Fine biomass burning BC and POC emissions were obtained by combining satellite-derived 8-day fuel burn data [*Giglio et al.*, 2006] with land use data (to determine fire type) and emission factors [*Andreae and Merlet*, 2001]. Fuel burn data for five separate years were used and repeated beyond five years in all simulations. Coarse BC and POC emissions (not shown in the table) for all sources in the model were estimated as 25% and 45% of those fine BC and POC emissions, respectively. The POM/POC emission ratio used was 1.6:1 for fossil fuels and 2:1 for biofuel and biomass burning. The emission rate of S(VI) from fossil fuels was 1% that of BC + POM + S(VI). Fossil fuel components were emitted into the EFFS distribution. Biofuel and biomass burning components were emitted into the IM distribution.

released, A_{cell} is the total horizontal area of the grid cell (cm²), F_r is the number of flashes per centimeter in the cloud, and t is time (s). For cloud-to-ground lightning, E_l ranges from $1.8-11$ GJ/flash, and values of F_{NO} range from 5 to 15×10^{16} molecules NO/J [*Price et al.*, 1997]. Combining these give $E_l F_{NO} = 9 \times 10^{25}-1.7 \times 10^{27}$ NO molecules per flash for cloud-to-ground lightning. A review by *Schumann and Huntrieser* [2007] suggests $E_l F_{NO} = 1.5$ $(0.2-4) \times 10^{26}$ NO molecules per flash to be consistent with satellite data. For this study, we assumed $E_l F_{NO} = 1.5 \times 10^{26}$ NO molecules per flash for both intracloud and cloud-ground lightning, since *Ridley et al.* [2005] suggest that the NO production per flash for intracloud lightning should be similar to that for cloud-to-ground lightning.

[13] The emission ratios of other gases to NO (molecules-gas per molecule-NO) during lightning were estimated as follows: NO_2: 0.076; N_2O: 0.000063; CO: 0.00028; HONO: 0.0067; HNO_3: 0.00024; H_2O_2: 0.00012; HO_2: 0.00012 [*Bhetanabhotla et al.*, 1985, Table 4]. These estimates account for emissions from channel heating for gases aside from N_2O and corona discharge for N_2O.

[14] The flash rate per unit distance in a cloud (dF_r/dt) (flashes cm⁻¹ s⁻¹) for intracloud (IC) lightning was calculated with

$$\left(\frac{dF_r}{dt}\right)_{IC} = \frac{1}{\Delta z_{max} E_{th}} \frac{dE_{f,max}}{dt} \qquad (2)$$

where $E_{f,max}$ is the maximum electric field strength (V/cm) within any vertical portion of the cloud of thickness Δz_{max} (cm), and E_{th} is the threshold electric field strength (V/cm) (which ranges from 1000 to 4000 V/cm, with an average assumed here of 3000 V/cm). Lightning occurs when $E_{f,max} > E_{th}$.

[15] The change in the maximum electric field strength with time was calculated as

$$\frac{dE_{f,max}}{dt} = \frac{2k_C}{\Delta z_{max} \sqrt{\Delta z_{max}^2 + R_c^2}} \frac{dQ_{b,max}}{dt} \qquad (3)$$

where $k_C = 8.98755 \times 10^{11}$ V cm C⁻¹ is Coulomb's constant, $R_c = \sqrt{F_c A_{cell}/\pi}$ is the horizontal radius (cm) of a cloudy region (in which F_c is the fractional cloudiness through the column), and $Q_{b,max}$ is the maximum charge separation (C) within a cloudy region. Equation (3) is similar to an equation from *Wang and Prinn* [2000], but with different methods of calculating charge separation and the portion of a cloud where separation occurs. The time rate of change of maximum charge separation was calculated here as

$$\frac{dQ_{b,max}}{dt} = F_c A_{cell} \sum_{m=K_{low}}^{K_{high}} \frac{dQ_{b,m}}{dt} \Delta z_m \qquad (4)$$

where $Q_{b,m}$ is the charge separation per unit volume of air (C cm⁻³) in model layer m between layers K_{low} and K_{high} in which the maximum net charge separation within the cloud occurs. $dQ_{b,max}/dt$ is determined by solving equation (4) between all possible combinations of K_{low} and K_{high} within a cloud, then taking the maximum of these values. This method appears physical since a flash should occur first where the field strength is greatest. Merely calculating the field strength between the top and bottom of the cloud always results in a field strength less than the maximum thus should underpredict lightning flashes.

[16] The time rate of change of $Q_{b,m}$ within a layer was determined by considering size-resolved coagulation boun-ceoffs with

$$\frac{dQ_{b,m}}{dt} = \left[\sum_{J=1}^{N_H} \sum_{j=1}^{N_C} \sum_{I=J}^{N_H} \sum_{i=j}^{N_C} \right.$$
$$\left. \cdot B_{Ii,Jj} \frac{\left(v_{Ii} n_{Ii,t} n_{Jj,t-h} + v_{Jj} n_{Ii,t-h} n_{Jj,t}\right)}{v_{Ii} + v_{Jj}} \Delta Q_{Ii,Jj} \right]_m \qquad (5)$$

where N_H is the number of hydrometeor size distributions, N_C is the number of size bins in each hydrometeor

Table 4. Natural Emission Rates and the Climate-Sensitive Parameters That Affected Them[a]

Emitted Gas or Particle	Model Climate-Sensitive Variables Affecting Emission	2000 Annual Emission	2030 A1B-2000 Annual Emission (%)	2030 B1-2000 Annual Emission (%)
Lightning NO	T, C, A	6.9 Tg N	−11.6	−2.6
Lightning NO_2	T, C, A	0.52 Tg N	−11.6	−2.6
Lightning HONO	T, C, A	0.047 Tg N	−11.6	−2.6
Lightning HNO_3	T, C, A	0.0017 Tg N	−11.6	−2.6
Lightning N_2O	T, C, A	0.00087 Tg N	−11.6	−2.6
Lightning H_2O_2	T, C, A	0.0020 Tg	−11.6	−2.6
Lightning HO_2	T, C, A	0.0020 Tg	−11.6	−2.6
Lightning CO	T, C, A	0.0039 Tg	−11.6	−2.6
Ocean DMS	W, T, SI	32.1 Tg	−1.41	−1.12
Ocean N_2O	W, T, SI	5.70 Tg	−1.41	−1.12
Ocean H_2	W, T, SI	3.53 Tg	−1.41	−1.12
Ocean CH_4	W, T, SI	15.1Tg	−1.41	−1.12
Ocean sea spray	W, T, SI	514 Tg	−0.44	+0.68
Ocean bacteria	W, T, SI	13.3 Tg	−0.43	+0.72
Soil NO	T, W	6.30 Tg N	+0.21	+1.61
Soil N_2O	T, W	10.26 Tg	+0.19	+1.61
Soil H_2	T, W	3.46 Tg	+0.20	+1.6
Soil/termite/rumin. CH_4	T, W	206 Tg	+0.19	+1.6
Soil H_2S	T	0.433 Tg	+0.74	+2.8
Soil DMS	T	0.539 Tg	+1.04	+3.3
Soil OCS	T	0.553 Tg	+0.092	+2.9
Soil CS_2	T	0.0468 Tg	+0.60	+3.3
Biogenic isoprene	T, P	457 Tg C	+0.75	+4.0
Biogenic monoterpenes	T	108 Tg C	+1.2	+5.1
Biogenic other VOC	T	212 Tg C	+0.09	+2.9
Biogenic CH_3OH	T, P	50 Tg C	+2.0	+2.1
Land bacteria	TKE, SC	28.1 Tg	+1.0	+0.19
Pollen	TKE, SC	84.5 Tg	+0.044	−0.27
Spores	TKE, RH, SC	186 Tg	+0.87	+0.87
Soil dust	W, T, SM, SC	7800 Tg	−0.18	−4.0
Volcanic SO_2 (#)	−	4.83 Tg S	+0	+0
Soil respiration CO_2	T, SM	47.2 Pg C	−0.50	+1.7
Plant respiration CO_2	T	65.0 Pg C	+0.36	+2.1
Gross Pri. Prod. (GPP)	T, RH, PAR	118 Pg C	+1.3	+2.1
Net Pri. Prod. (NPP)	T, RH, PAR	53.4 Pg C	+2.4	+2.2
Wildfires	−	*	*	*

[a]T, air temperature; RH, relative humidity; W, wind speed; TKE, turbulent kinetic energy; SM, soil moisture; SI, sea ice cover; SC, snow cover; P, photosynthetically active radiation (PAR); C, cloud size distributions; A, aerosol size distributions; OT, ocean temperature; OC, ocean composition. #, other volcanically emitted chemicals (and their emissions, in Tg/a) were H_2O (25.2), CO_2 (9.0), HCl (6.7), HBr (0.21), CO (0.22), OCS (0.21), CS_2 (0.21), H_2S (2.65), H_2 (0.05), S(VI) (0.33), Na^+ (0.50), Ca^{2+} (0.25), K^+ (0.43), and soildust (0.95). *, total biomass burning emissions of BC and POC were given in Table 2. Emissions of other gases and particle constituents from biomass burning were derived as described in section 3.1. Wildfire emissions are about 10% of the total biomass burning.

distribution, n is the number concentration of hydrometeor particles per size bin per distribution (particles cm^{-3}), υ is the volume of a single particle (cm^3 $particle^{-1}$), $B_{Ii,Jj,m}$ is the bounceoff rate (cm^3 $particle^{-1}$ s^{-1}) of a particle in size bin i of hydrometeor distribution I bouncing off a particle in size bin j of hydrometeor distribution J in any cloud layer m, and $\Delta Q_{Ii,Jj}$ is the charge separation per bounceoff (Coulombs per bounceoff).

[17] In the present application, $N_C = 30$ size bins and $N_H = 3$, where the distributions were liquid, ice, and graupel, respectively. Bounceoffs and charge separation between and among particles in all three hydrometeor distributions were considered. Hydrometeor number concentrations in each size bin were predicted. The bounceoff rate was

$$B_{Ii,Jj} = \left(1 - E_{coal,Ii,Jj,m}\right)K_{Ii,Jj,m} \quad (6)$$

where $K_{Ii,Jj,m}$ is the collision kernel (cm^3 $particle^{-1}$ s^{-1}) and $E_{coal,Ii,Jj,m}$ is a dimensionless coalescence efficiency. Colli-

sion kernels are provided in *Jacobson* [2005b, Section 15.6]. Coalescence efficiencies were determined for different size regimes from the parameterizations of *Beard and Ochs* [1984], *Low and List* [1982], and *Pruppacher and Klett* [1997, equations (14)–(28)]. The charge separation per bounceoff due to the thermoelectric rebound charging mechanism was calculated as the smaller of the charges available on two colliding particles

$$\Delta Q_{Ii,Jj} = \min\left(Q_{Ii}, Q_{Jj}\right) \quad (7)$$

where Q_{Ii} and Q_{Jj} are the maximum charges (C) on single particles of a given size. *Pruppacher and Klett* [1997] give $Q_{Ii} = f \times 3.333 \times 10^{-10} \times 2r_{Ii}^2$ as a fit through data for the most highly electrified, precipitating clouds and $Q_{Ii} = f \times 3.333 \times 10^{-10} \times 0.0005r_{Ii}^{1.3}$ as a fit through data for electrified warm clouds (equations for Q_{Jj} are similar), where r_{Ii} is particle radius in cm, $2r_{Ii}^2$ has units of esu, 3.333×10^{-10} is the number of Coulombs per esu, and f is a fraction
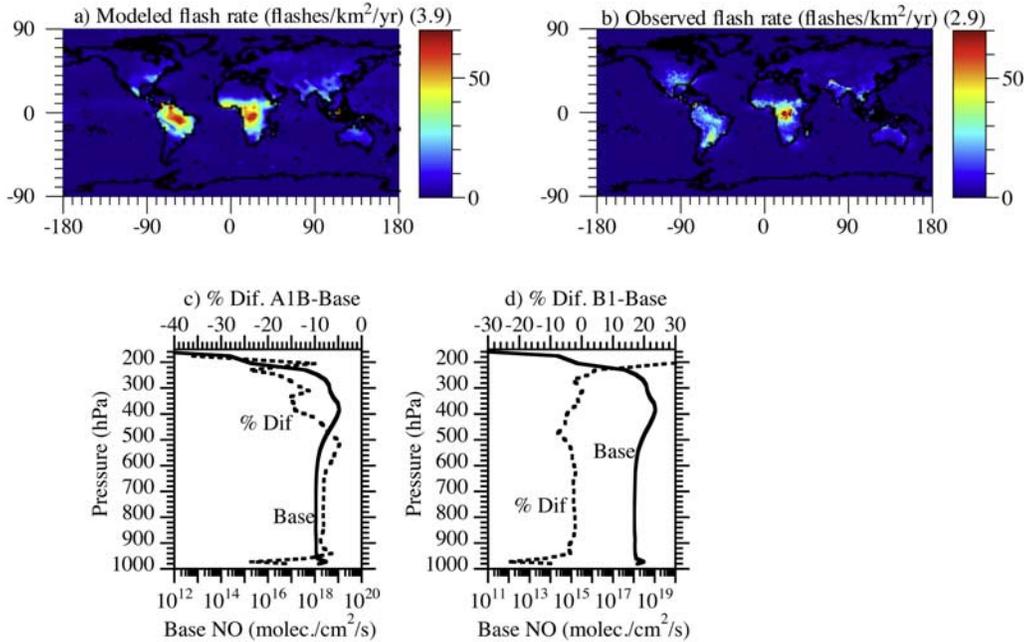
Figure 1. (a) Modeled ($4° \times 5°$ resolution) and (b) 1995–2005 observed ($0.5° \times 0.5°$ resolution [*GHCC*, 2008]) annual intracloud plus cloud-ground lightning flash rate (flashes/km^2/a). Numbers in parentheses are global averages. (c, d) Modeled vertical profiles of globally averaged and simulation-averaged NO$_x$ production from lightning in the base case and percentage differences between the A1B and base case and the B1 and base case.

assigned here to account for the fact that the fits were through data for highly charged clouds rather than average clouds. We assumed $f = 0.2$ for the ice, graupel, and liquid cloud distributions, based on an eyeball estimate of the factor needed to adjust the equations to fit average rather than maximum charge data for large particle size in Figure 18-1 of *Pruppacher and Klett* [1997]. The equations and data indicate that the charge per particle on an ice crystal exceeds that on a liquid drop; thus charge separation due to rebounding ice crystals exceeds that due to rebounding liquid drops.

[18] Finally, the flash rate for cloud-to-ground (CG) lightning was estimated as

$$\left(\frac{dF_r}{dt}\right)_{CG} = \frac{1}{2.7\sqrt{R_f}}\left(\frac{dF_r}{dt}\right)_{IC} \qquad (8)$$

where $R_f = \max[(dE_f/dt)/E_{th}, 1]$ is the intracloud flash rate (flashes/min.) [*Rutledge et al.*, 1992]. The lower limit $R_f = 1$ flash/min. is the lower bound of the data.

[19] One limit was placed on lightning formation to prevent excessive lightning over the oceans and at high latitudes. This problem arises because the cumulus parameterization for cloud thermodynamics does not treat tilted updrafts, uses a coarse time step, and does not resolve the width of clouds (as with all global models). The limit was to allow lightning to occur only when the cloud thickness exceeded a threshold. The threshold was selected by trial and error to be 8 km over all land, 13 km over the tropical ocean, and 11 km over the extratropical ocean. Most other studies to date have treated lightning following *Price and*

Rind [1992], who parameterized the flash rate as an empirical function of cloud top height, with different functions over the ocean and land. Here the lightning flash rate is a function of the bounceoff rate among size-resolved liquid and ice; thus it would not be a prognostic microphysical treatment if it determined flash rate from cloud top height. However, it can use cloud thickness to limit when lightning forms. Another method could be to use the height above the freezing level [e.g., *Futyan and Del Genio*, 2007].

[20] Figure 1 compares the modeled versus observed [*GHCC*, 2008] global distribution of the lightning flash rate. The observed global maximum lightning flash rate occurs over central Africa. Despite a factor of 80 lower area resolution than the data ($0.5° \times 0.5°$), the model ($4° \times 5°$) replicates the peak quite well. Other observed high lightning flash rates occur over much of South America, southeast Asia, northern Australia, and the southeast U.S. The model predicted strong peaks in the same areas, although the location of the modeled peak over South America is to the north of the observed peak and the spatial extent of the modeled peak over the southeast U.S. is lower than that of the observed peak there. However, other lightning data sets [e.g., *Tie et al.*, 2002, Figure 1] show the observed South America peak in the same location as the present modeled peak and a lower measured flash rate over the southeast U.S. than shown in the present Figure 1. The model predicted some lightning off the Atlantic coast of the U.S., as seen in the observations.

[21] *Ridley et al.* [2005] estimated global NO$_x$ production from lightning as 2–20 Tg N/a. *Schumann and Huntrieser* [2007] refined this to 2–8 Tg N/a, and *Martin et al.* [2007],

to 4–8 Tg N/a. Here NO_x ($NO+NO_2$) lightning production was 7.4 Tg N/a (6.9 from NO; 0.5 from NO_2) for the base case (Table 4), within all three ranges. *Christian et al.* [2003] derived global, land, and ocean flash rates of 44, 31–49, and 5 flashes/s, respectively. The corresponding numbers here were 63 (global), 55 (land), and 7.9 (ocean) flashes/s, respectively, very close to the ocean observation but with greater error over land. The changes in NO from lightning in the A1B and B1 scenarios were only about 2% and 4%, respectively, of the changes in NO from anthropogenic sources in those scenarios (Tables 2 and 4).

[22] It was found here that the lightning flash rate is affected significantly by the coalescence efficiency of medium-sized hydrometeor particles colliding with large particles. For a given 4 mm diameter drop, for example, the coalescence efficiency decreases from about 0.7 for collisions with a 250 μm drop to 0 for collisions with a 1 mm drop [*Low and List*, 1982, Figure 8]. Since (1) clouds reach great heights and many drops become large over central Africa, (2) many large-drop interactions have low coalescence efficiencies, and (3) charge separation increases with decreasing coalescence efficiency, the low coalescence efficiency of large drops may explain much of the high lightning occurrence over central Africa. This hypothesis is supported by a simulation in which the coalescence efficiencies of *Low and List* [1982] for large drop interactions were set to unity (but other efficiencies were calculated as before). In that case, very little lightning formed over central Africa.

[23] Figures 1c and 1d show the modeled vertical profile of globally and simulation-averaged NO production from lightning and the percent differences between the future cases and the base case. It indicates two peaks, one in the middle-upper troposphere and another below 1 km (900 hPa). Two major peaks are also seen in the observed vertical profiles by *Pickering et al.* [1998], one below 1 km and the other above 7 km. Once lightning-NO is produced, cloud convection lifts much of the NO, as well as boundary layer-NO to the anvils, so the location of lightning production is not necessarily the same as the location of where NO is observed, which is often in anvil regions [e.g., *Hauglustaine et al.*, 2001].

3.3. NO, N_2O, H_2, CH_4, H_2S, DMS, OCS, and CS_2 From Soils

[24] Soil NO emissions were obtained by combining 1-km vegetation fraction and landuse class data (BELD3 from *USEPA* [2006] for the U.S. and *USGS* [1999] for the rest of the world) with emission factors for each of 24 USGS landuse classes [*USEPA*, 2006] to determine normalized (at a specific temperature) emission rates of soil NO.

[25] Normalized NO emission rates were then combined with temperature-, canopy-, turbulence-, and wind speed-dependent, equations to determine instantaneous emission rates (molec. cm^{-2} s^{-1}) with

$$E_{NO,soil} = E_{NO,n} e^{-(AT-B)} \left[f_{NO} + (1-f_{NO}) \sum_{k=1}^{N_l} f_{l,k} \frac{\alpha v_{c,k}}{\alpha v_{c,k} + v_{d,k}} \right] \tag{9}$$

where $E_{NO,n}$ is the normalized emission rate at 306.78 K, T is Kelvin temperature, $A = 0.05112$, $B = 15.68248$ (from BELD3), N_l is the number of landuse categories in a grid cell, $f_{l,k}$ is the fractional area of a grid cell in each landuse category, $v_{c,k}/(v_{c,k} + v_{d,k})$ is the fraction of soil-emitted NO ventilated through a canopy to the free atmosphere in landuse class k, and f_{NO} is the fraction of NO that does not oxidize to NO_2 in the canopy. Following *Wang et al.* [1998], $f_{NO} = 0.7$. The remaining NO is oxidized to NO_2, a portion of which is deposited within the canopy. The parameter

$$v_{c,k} = \min \left[v, \frac{v}{\gamma_k \sqrt{L_{T,k}}} \right] \tag{10}$$

is the in-canopy wind speed (m/s) in landuse class k, which is a function of the grid-cell averaged above-canopy wind speed (v, m/s), the one-sided leaf area index (L_T, m^2 leaf/m^2 ground), and a nondimensional extinction coefficient characterizing the decrease of wind speed with depth in the canopy (1, 2, 4 for grass, shrub, forest ecosystems, respectively). The leaf area index in the model varied monthly and was interpolated for subgrid soil classes from 1-km resolution satellite data [*USGS*, 2008]. The parameter α is a dimensionless coefficient with values 0.028 and 0.0056 for day and night, respectively [*Wang et al.*, 1998, and references therein]. Finally, $v_{d,k}$ is the in-canopy dry deposition speed of NO_2 (m/s) in landuse class k, estimated here as

$$v_{d,k} = \frac{1}{R_a + R_b + R_{s,k}} \tag{11}$$

where R_a, R_b, and $R_{s,k}$ are the aerodynamic resistance, resistance to molecular diffusion through the laminar sublayer, and canopy surface resistance (s/m) against NO_2 loss [e.g., *Jacobson*, 2005b, chapter 20].

[26] N_2O, H_2, and CH_4 emissions from soils and (for CH_4), natural ruminants and termites, were calculated versus temperature, wind speed, and landuse by scaling modeled time-varying soil NO emissions (above) to preestimated global natural N_2O:NO, H_2:NO, and CH_4:NO emission ratio estimates. For the ratios, 6.5 Tg N/a of NO (based on a 10-year simulations), 6.6 Tg N/a of N_2O [*Bouwman et al.*, 1995], 3.5 Tg H_2 [*Sanderson et al.*, 2003], and 208 Tg CH_4/a [*Warneck*, 1999] were assumed.

[27] H_2S, DMS, OCS, and CS_2 emission rates for soils were calculated as a function of temperature and landuse type (agricultural, grassland/rangeland, forest, and wetland) with empirical equations based on measurements by *Lamb et al.* [1987].

3.4. Isoprene, Monoterpenes, Methanol, and Other VOCs From Vegetation

[28] Emission rates of isoprene, monoterpenes, and other volatile organic compounds were determined by combining 1-km vegetation fraction and landuse class data (BELD3: *USEPA* [2006] for the U.S. and *USGS* [1999] for the rest of the world) with emission factors (g C/km^2/hr) for each of 24 USGS landuse classes [*USEPA*, 2006] to determine normalized (at 303.15 K and 1000 um/m^2/s photosynthetically active radiation, PAR) emission rates. For each model grid

cell, the normalized emission rate for each gas was determined by summing the product of the emission factor and the fractional area of each landuse class, determined from the vegetation fraction data.

[29] The normalized emissions were combined with modeled time-, temperature- and PAR-dependent adjustments. For isoprene, the adjustments accounted for temperature, direct PAR, diffuse PAR, and one-sided leaf area index [*Guenther et al.*, 1995]. Direct and diffuse PAR were calculated by solving radiative transfer through clouds, aerosols, and gases in 32 wavelength intervals between 400 and 700 nm. For monoterpenes and other volatile organics, adjustments accounted for temperature only.

[30] *Guenther et al.* [1995] estimated global isoprene, monoterpene, and other reactive VOC emissions as 506, 127, and 259 Tg C/a, respectively. *Liao et al.* [2006] estimated these values as 437.9, 117, and 260 Tg C/a, respectively. The results calculated here are 457, 108, and 212 Tg C/a, respectively (Table 4).

3.5. Ocean DMS, N_2O, H_2, and CH_4

[31] Emissions of dimethylsulfide (DMS) were calculated as a function of wind speed, temperature, and seawater concentration. DMS seawater concentrations were obtained from data by *Kettle et al.* [1999]. The transfer velocity was calculated as in the work of *Wanninkhof* [1992].

[32] Ocean N_2O, H_2, and CH_4 emissions were calculated versus wind speed, temperature, and seawater concentration by scaling modeled time-dependent ocean DMS emissions (above) to global ocean N_2O:DMS, H_2:DMS, and CH_4:DMS emission ratio estimates calculated from 31.8 Tg DMS/a (based on a 10-year model calculation), 3.6 Tg N/a of N_2O [*Bouwman et al.*, 1995], 3.5 Tg-H_2/a [*Sanderson et al.*, 2003], and 15 Tg CH_4/a [*Karl et al.*, 2008]. Thus ocean N_2O, H_2, and CH_4 were time-dependent but proportional to DMS emissions.

3.6. Sea Spray

[33] Sea spray emissions were calculated as a function of size and wind speed by *Clarke et al.* [2006] for drops <4 μm and *Smith and Harrison* [1998] for drops 4–1000 μm. Emissions were also affected by sea ice and fall speed, which were climate dependent. The composition of sea spray was determined over time and in the three-dimensional ocean by solving ocean chemical equilibrium equations together with nonequilibrium ocean-atmosphere exchange equations for all atmospheric gases [*Jacobson*, 2005c]. Sea spray–related chemicals emitted into the internally mixed (IM) aerosol distribution (Table 1) included $H_2O(l)$, POM, H^+, Na^+, Cl^-, NO_3^-, $H_2SO_4(aq)$, HSO_4^-, and SO_4^{2-}. Also, K^+, Ca^{2+}, Mg^{2+}, Li^+, and Sr^{2+} were emitted as mole equivalent Na^+; $H_2PO_4^-$, HPO_4^{2-}, PO_4^{3-}, $B(OH)_4^-$, $SiO(OH)_3^-$, F^-, and Br^- were emitted as mole equivalent Cl^-.

[34] Because the center of the lowest model layer was about 38 m above sea level and large sea spray/spume drop particles fall quickly to the ocean before reaching this height, it was necessary to calculate an effective emission rate of drops from 10 m above the surface to the middle of the lowest model layer. This was accomplished by first calculating the time-dependent concentration of sea spray

versus size at 10 m, assuming that only emission and gravitational settling occur, from

$$\frac{dn_{r,i}}{dt} = \frac{E_{o,i}}{z_r} - n_{r,i}\frac{v_{f,i}}{z_r} \tag{12}$$

where $n_{r,i}$ is the number concentration (particles cm^{-3}) of sea spray drops of size i reaching reference height z_r (1000 cm), $E_{o,i}$ is the emission rate at the ocean surface (particles cm^{-2} s^{-1}), and $v_{f,i}$ is the fall speed of the particles (cm s^{-1}), determined as a function of temperature and other parameters [*Jacobson*, 2005b, chapter 20]. The analytical solution to this equation over time step h (s) is

$$n_{r,i} = \frac{E_{o,i}}{v_{f,i}}\left(1 - e^{-hv_{f,i}/z_r}\right) \tag{13}$$

The emission rate (particles cm^{-2} s^{-1}) to the middle of the bottom layer is then

$$E_{m,i} = \frac{z_r}{h}n_{r,i} \tag{14}$$

This treatment smoothly eliminates large direct injections of sea spray or spume drops into the middle of the bottom model layer. Such injections are erroneous because the fall speed of such drops should remove them prior to injection to that altitude.

3.7. Soil Dust

[35] Soil dust emissions versus size, soil type, and wind speed were calculated by *Marticorena et al.* [1997] using FAO [1995] soil data. Soil dust emissions were also a function of soil moisture and snow cover. Like with sea spray, soil dust emissions into the middle of the lowest model layer were calculated with equations (12)–(14).

3.8. Bacteria, Spores, and Pollen

[36] Bacteria live in water, soil, and plants. Spores are reproductive or resting organisms released by fungi and algae growing on leaf surfaces or soil. Pollen are large granules containing male genetic material released from flowers and windblown to other flowers for fertilization. Bacteria, spores, and pollen serve as cloud condensation nuclei [e.g., *Bauer et al.*, 2003] and sites for aerosol condensation. Previous model studies of bacteria, spores, or pollen considered only their regional transport assuming fixed emissions [e.g., *Pasken and Pietrowicz*, 2005]. Biological emissions, though, depend on turbulence, gustiness, temperature, and relative humidity [e.g., *Eversmeyer et al.*, 1971; *Aylor and Parlange*, 1975; *Shaw et al.*, 1979; *Carisse and Philion*, 2002; *Mouli et al.*, 2005].

[37] Here bacteria, spore, and pollen emissions were estimated by accounting for their dependences on some climate parameters. Whereas spores and pollen were assumed to be emitted from leaf surfaces, land bacteria were assumed to be emitted from soils. Size-distributed ocean bacteria emissions were estimated conservatively as 0.5% that of sea spray particle emissions by number, following *Posfai et al.* [2003] who measured bacteria as 1% by number over the southern Pacific Ocean. Sea spray, thus ocean bacteria,

Table 5. Factors Used for Pollen, Spore, and Bacteria Emission Rates[a]

Month (NH)	Pollen	Spores	Bacteria	Hour of day	Pollen	Hour of day	Pollen
1	0.5	0.5	0.6	0−1	0.1	12−13	1.5
2	0.5	0.5	0.6	1−2	0.1	13−14	1
3	0.5	0.5	0.6	2−3	0.1	14−15	0.5
4	2.0	1.5	0.6	3−4	0.1	15−16	0.4
5	2.0	1.5	1.4	4−5	0.1	16−17	0.3
6	2.0	1.5	1.4	5−6	0.2	17−18	0.2
7	1.0	1.5	1.4	6−7	4	18−19	0.1
8	1.0	1.5	1.4	7−8	4	19−20	0.1
9	1.0	1.5	1.4	8−9	3.3	20−21	0.1
10	0.5	0.5	1.4	9−10	3	21−22	0.1
11	0.5	0.5	0.6	10−11	2.5	22−23	0.1
12	0.5	0.5	0.6	11−12	2.	23−24	0.1

[a](left) Factor to multiply pollen, spore, or bacteria emission rates by to account for the monthly variation of their emissions in the Northern Hemisphere (for the Southern Hemisphere, offset values by 6 months). The sum of each factor, over all months in a year, is 12. Data for spores were estimated from the work of *Sakiyan and Inceoglu* [2003]; those for bacteria were estimated from the work of *Bovallius et al.* [1978]. (right) Same as the left, but for each hour of the day in the case of pollen. The sum of all fractions is 24. Derived from data by *Ogden and Hayes* [1969].

emissions in the model depended on wind speed, temperature, and sea ice.

[38] Since emissions of land bacteria, spores, and pollen depend on gustiness rather than mean wind speed [*Eversmeyer et al.*, 1971], their emission rates were assumed here to be proportional to turbulent kinetic energy (TKE). TKE also conveniently accounts for buoyancy, which peaks when temperatures reach their maximum during the day. Relative humidity was further assumed to affect spore emissions [*Carisse and Philion*, 2002].

[39] Soil bacteria emissions (colony-forming units (CFUs)/cm² ground/s) into a given aerosol size bin i in a model grid cell were estimated with

$$E_{lb,i} = E_{lb,\max} R_{TKE} R_{m,lb} R_{n,i,lb} \sum_{j=1}^{N_s} f_{v,j} \qquad (15)$$

where $E_{lb,\max}$ is the maximum estimated yearly averaged bacteria emission rate (CFUs/cm² ground/s)

$$R_{TKE} = \exp[\min(TKE - TKE_{\lim}, 0)] \qquad (16)$$

is a factor varying between 0 and 1 accounting for the assumed variation of emission with model-predicted turbulent kinetic energy (TKE, m²/s²) relative to the TKE that gives the maximum emission rate ($TKE_{\lim} = 1$ m²/s²), $R_{m,lb}$ is a factor (Table 5a) accounting for the monthly variation of bacteria emissions

$$R_{n,i,lb} = \frac{\Delta d_i}{d_i \sqrt{2\pi} \ln \sigma_{g,lb}} \exp\left[-\frac{\ln^2\left(d_i/\overline{D}_{N,lb}\right)}{2 \ln^2 \sigma_{g,lb}}\right] \qquad (17)$$

is the fraction of the total bacteria number emitted into internally mixed (IM) (Table 1) aerosol size bin i according to a lognormal distribution (where d_i is particle diameter, $\sigma_{g,lb}$ is geometric standard deviation, and $\overline{D}_{N,lb}$ is geometric mean number diameter), N_s is the number of soil classes in each model grid cell, and $f_{v,j}$ is the vegetation fraction of each soil class in each cell. Emitted bacteria are generally 0.5−10 μm in diameter. Here $\overline{D}_{N,lb} = 2$ μm and $\sigma_{g,lb} = 1.37$.

Bacteria releases tend to increase in the late spring, summer, and early autumn [e.g., *Bovallius et al.*, 1978]. The maximum yearly averaged emission rate was estimated as $E_{lb,\max} = 0.8$ CFUs/cm²/s. This results in a maximum steady state concentration, according to equation (13), of 4000 CFUs/m³, when the wind speed (substituted for fall speed in equation (13)) is 2 m/s and $R_{TKE} = 1$, $R_{m,lb} = 1.4$, and $f_{v,j} = 1$. This is close to the upper measured values of 4000−8500 CFUs/m³ reported by *Shaffer and Lighthart* [1994]. Since *TKE* and vegetation fraction are almost always smaller than their maximum values, this maximum rate was rarely realized in the model.

[40] Spore emissions from plants and trees into an aerosol size bin (spores/cm² leaf area/s) were estimated with

$$E_{sp,i} = E_{sp,\max} R_{TKE} R_{RH} R_{m,sp} R_{n,i,sp} \sum_{j=1}^{N_s} L_{T,j} f_{v,j} \qquad (18)$$

where $E_{sp,\max}$ is the maximum yearly averaged emission rate (spores/cm² leaf area/s),

$$R_{RH} = \min[(1.15 - RH)/0.5, 1.0] \qquad (19)$$

is a factor, estimated from data by *Carisse and Philion* [2002] and varying between 0.3 (at $RH = 1.0$) and 1 (at $RH = 0.65$), that accounts for the assumed linear variation of emissions with model-predicted relative humidity (RH, fraction). $R_{m,sp}$ is a factor (Table 5a) accounting for the monthly variation in spore emissions, and

$$R_{n,i,sp} = \frac{\Delta d_i}{d_i \sqrt{2\pi} \ln \sigma_{g,sp}} \exp\left[-\frac{\ln^2\left(d_i/\overline{D}_{N,sp}\right)}{2 \ln^2 \sigma_{g,sp}}\right] \qquad (20)$$

is analogous to equation (17). Emitted spores are generally 2−3.5 μm in diameter with a density of 0.56 to 1.44 g/cm³. Here $\overline{D}_{N,sp} = 3$ um and $\sigma_{g,sp} = 1.2$ [*Reponen*, 1995]. The latitudinal dependence of spore emissions is accounted for in the variation of leaf area index with latitude.

[41] The maximum yearly averaged spore emission rate was estimated as $E_{sp,\max} = 0.2$ spores/cm² leaf area/s.

Multiplying through by $R_{TKE} = 1$, $R_{RH} = 1$, $R_{m,sp} = 1.5$ (Table 5a), $f_{v,j} = 1$, and $L_T = 7 \text{ m}^2/\text{m}^2$ and applying the result to equation (13) with a wind speed of 1 m/s gives a maximum steady state spore concentration of 21,000 spores/m^3, conservatively below the instantaneous measured upper limit of 170,000 spores/m^3 [*Burch and Levetin*, 2002] and above the maximum monthly average (August) in Ankura of 5800 spores/m^3 [*Sakiyan and Inceoglu*, 2003].

[42] Pollen emissions from plants and trees into a size bin (pollen grains/cm^2 leaf area/s) were estimated with

$$E_{po,i} = E_{po,\max} R_{TKE} R_{h,po} R_{m,po} R_{n,i,po} \sum_{j=1}^{N_s} L_{T,j} f_{v,j} \qquad (21)$$

where $E_{po,,\max}$ is the maximum emission rate (pollen grains/cm^2 leaf area/s), $R_{m,po}$ and $R_{h,po}$ (Table 5) account for monthly and hourly variations in pollen emissions, and

$$R_{n,i,po} = \frac{\Delta d_i}{d_i \sqrt{2\pi} \ln \sigma_{g,po}} \exp\left[-\frac{\ln^2 \left(d_i / \overline{D}_{N,po} \right)}{2 \ln^2 \sigma_{g,po}} \right] \qquad (22)$$

is analogous to equation (17). Pollen releases generally occur heavily in the morning, when plant surfaces dry and turbulence increases. Releases decrease during the day as the source of pollen diminishes [e.g., *Ogden and Hayes*, 1969]. Pollen is often released more in spring than other months [e.g., *Pasken and Pietrowicz*, 2005]. Table 5 accounts for these factors. The latitudinal dependence of pollen emissions is accounted for in the variation of leaf area index with latitude. Emitted pollen grains are generally large, ranging from 10 to 125 μm in diameter. Here $\overline{D}_{N,po} = 30$ um and $\sigma_{g,po} = 1.4$. The maximum emission rate was estimated conservatively as $E_{po,\max} = 0.00005$ pollen grains/cm^2 leaf area/s, or 16 million grains/m^2 leaf area/a. A typical corn plants emits 14–50 million grains/plant/a (all within a short period [*Miller*, 1985]). With 20,000 corn plants per acre (4.94 plants/m^2 land) and a typical leaf area index for corn of 5 m^2/m^2, each corn plant has about one square meter of leaf area, thus the upper limit of modeled corn pollen emissions is 16 million grains/plant/a.

3.9. CO$_2$ Photosynthesis/Respiration, Ocean-Atmosphere Exchange, and Biogenic CH$_3$OH

[43] The model treated CO$_2$ uptake by plants via photosynthesis, CO$_2$ emissions by plants and soils via respiration, and CO$_2$ exchange with the oceans. C$_3$ plant photosynthesis and mitochondrial respiration were modeled after the work of *Farquhar et al.* [1980] with updates for temperature dependence by *Collatz et al.* [1991] and *Bernacchi et al.* [2003]. Photosynthesis and mitochondrial respiration in C$_4$ plants and their temperature dependences were modeled after the work of *Collatz et al.* [1991, 1992]. Calculations for C$_3$ and C$_4$ plants required an iteration to determine stomatal conductance, CO$_2$ uptake by leaves, and intercellular CO$_2$ and depended on PAR, temperature, and the relative humidity. Soil heterotrophic bacteria respiration depended on temperature, soil moisture, and soil type [from *FAO*, 1995] after the data by *Howard and Howard* [1993].

[44] Methanol emissions from grass and plants growth and decay were estimated following *Jacob et al.* [2005],

who calculate such emissions proportional to net primary production (NPP) and soil respiration, respectively. Here we calculated NPP and respiration directly, thus CH$_3$OH emissions depended on temperature, the relative humidity, and PAR.

[45] CO$_2$ ocean atmosphere exchange was calculated over time by solving nonequilibrium ocean atmosphere exchange coupled with ocean equilibrium chemistry [*Jacobson*, 2005c]. CO$_2$ exchange depended on air temperature, wind speed, ocean pH, and ocean carbon content, the latter two of which depended on ocean composition determined by the equilibrium solver. Photosynthesis/respiration over the oceans was not accounted for.

3.10. Volcanic and Wildfire Emissions

[46] Sporadic and continuous volcanic emissions and wildfire emissions were climate sensitive here only with respect to the height to which volcanic and biomass burning plumes could rise, which was a function of the temperature profile. Species emitted from volcanos include the gases SO$_2$, H$_2$O, CO$_2$, H$_2$, CO, H$_2$S, OCS, CS$_2$, HF, HCl, and HBr, and the particle components H$_2$SO$_4$(aq), HSO$_4^-$, SO$_4^{2-}$, Na$^+$, Ca^{2+}, K$^+$, and ash (treated as soildust in the model). SO$_2$ emissions originated from the work of *Andres and Kasgnoc* [1998]. Emissions of the other components were scaled using data from several studies.

[47] Chemicals emitted during wildfires were the same as those emitted during biomass burning (section 3.1). Biomass burning and wildfire emissions (treated through the same emission inventory) were assumed to alter the temperature (K) of the air each time step through

$$\Delta T_{bb} = \frac{E_{C,bb} H_w h}{f_C c_{p,m} \rho_a \Delta z} \qquad (23)$$

where $E_{C,bb}$ is the emission rate of carbon from biomass burning (kg C m^{-2} s^{-1}), $f_C = 0.45$ is the mass fraction of carbon in wood, H_W is the energy content of wood (1.361 $\times$ 10^7 J kg^{-1}), $c_{p,m}$ is the specific heat of moist air at constant pressure (J kg^{-1} K^{-1}), ρ_a is the mass density of air (kg m^{-3}), Δz is the height of the lowest model layer (m), and h is the time step (s). Although biomass burning plumes lofted above the bottom model layer, all burning occurred within the bottom layer, so equation (23) was applied there. Because it was not possible to separate anthropogenic from wildfire burning in the satellite-derived fuel-burn inventory (Table 3, caption), we did not calculate the feedback of climate change to wildfire emissions although this is an important topic for future work.

3.11. Future Emissions

[48] To develop future emissions, we supplemented the energy and emission forecasts developed by the Intergovernmental Panel on Climate Change (IPCC) for the Third Assessment Report [*Nakicenovic et al.*, 2000; *IPCC*, 2001]. The IPCC forecasts energy use by world region to 2100 in 10-year time steps, along several "marker" scenario trajectories that sketch different pathways of future societal development. We selected two scenarios, A1B and B1, between 2000 and 2030.

[49] Twenty-seven species and carbon bond IV (CB-IV) groups were projected. These included gases (NO, NO$_2$,

(a)

(b)
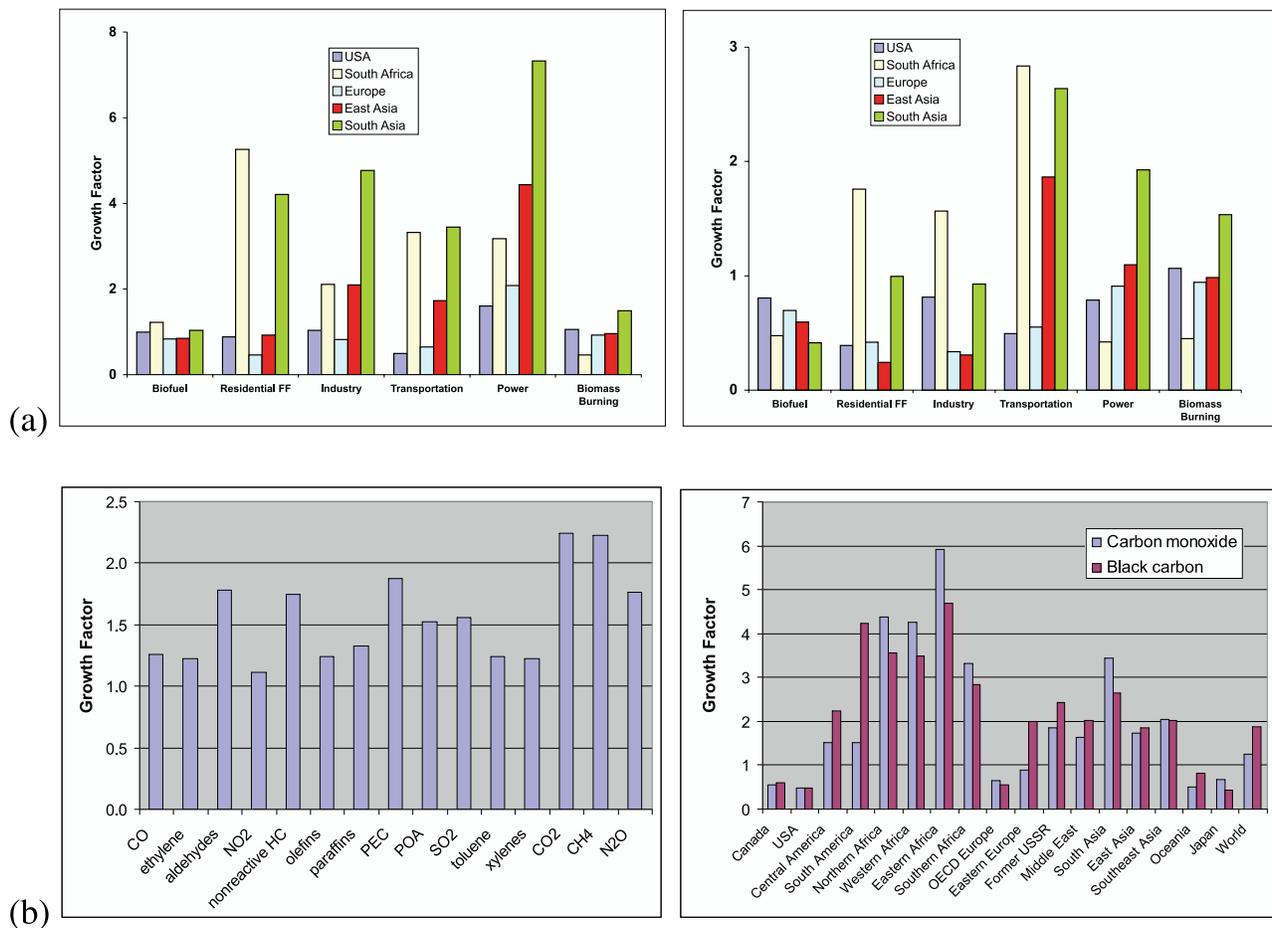
Figure 2. (a) 2000–2030 A1B growth factors by sector for selected world regions: (left) CO and (right) BC. (b) 2000–2030 A1B transportation sector growth factors (left) globally averaged by chemical species and (right) regionally averaged for CO and BC.

N_2O, NH_3, SO_2, H_2SO_4, CO, CO_2, CH_4, C_2H_4, HCHO, higher aldehydes, C_5H_8, terpenes, nonreactive VOCs, paraffins, olefins, ketones, alcohols, toluene, xylene) and aerosol components (BC, POC, sulfate, nitrate, fine PM, and coarse PM). We used the IMAGE model [*RIVM*, 2001] to disaggregate IPCC A1B and B1 forecasts of CO_2, CH_4, N_2O, SO_2, CO, VOC, and NO_x into 17 world regions for greater spatial resolution. VOC emissions were then speciated with profiles from the works of *Streets et al.* [2003a] and *Klimont et al.* [2002] for 82 emitting source types, linking IPCC energy use and other activities to organic emissions. Emissions of BC and POC were obtained from data by *Streets et al.* [2004]. Biomass burning estimates built on IPCC estimates for managed forests (slash-and-burn agriculture, etc.), an interpretation of natural biomass burning in mature forests specified by the IPCC, and an inventory of global biomass burning [*Bond et al.*, 2004; *Streets et al.*, 2003b; *Woo et al.*, 2003]. We used emission factors for vegetation burning from data by *Andreae and Merlet* [2001].

[50] 2000–2030 A1B and B1 emission growth factors were calculated for 27 chemicals, 17 world regions, and 8 emission sectors. These factors were applied to the base year model inventory to yield future year inventories. Figure 2a shows A1B factors for CO and BC by world region and emission sector. A1B growth factors for biofuel use and open biomass burning are small, and cluster around 1 (no change). CO growth is large in most other economic sectors, particularly the power sector, in the developing world, and low or declining in the developed world. BC emissions grow in the developing world transportation sector and decline in the developed world. Figure 2b (left) shows the average A1B transportation sector growth factors over all world regions for 15 chemicals. Growth is highest for CO_2 and CH_4, and varies from 1.1–1.8 for other species. Figure 2b (right) shows CO and BC A1B growth factors for all world regions in the transportation sector. Growth in the developing world, which increases 100–600%, differs from that in the developed world, which decreases up to 50% [*Streets et al.*, 2004].

[51] Table 2 shows the baseline and projected 2030 annual anthropogenic gas emissions and Table 3 shows the baseline and projected 2030 black carbon and organic carbon emissions used here. The 2030 projections were obtained by applying the future emission factors developed to the gridded baseline emission data. Globally, the A1B scenario produced more emissions than did the B1 or baseline scenario. The B1 scenario produced more global emissions of organic gases and carbon dioxide than the

baseline case, but lower emissions of other gases, BC, and POC.

4. Comparisons With Data

[52] Three 10-year equilibrium global climate simulations (4 × 5 degree resolution) were run: (a) baseline c. 2000 emissions, (b) A1B 2030 emissions, and (c) B1 2030 emissions. Longer simulations (e.g., 20 years) were not run due to limited computer resources and time. Thus the results here are relatively transient and provide information only as to the short-term effects of the different emission scenarios.

[53] Figure 3a compares baseline global fields precipitation with data. Figures 3b–3d compare surface ozone, vertical ozone profiles, and vertical temperature/dew point profiles, respectively with paired-in-space (e.g., model values in the exact location of the measurement) monthly data. The comparisons indicate extremely good agreement considering the coarseness of the model resolution. The model has also been compared previously with paired-in-time-and-space aircraft spiral and surface data for numerous parameters by *Jacobson* [2001b] and other studies.

5. Effects on Meteorological, Radiative, Aerosol, Cloud, and Lightning Variables

[54] Here A1B and B1 simulation results are compared with baseline results. Table 6 summarizes baseline values and differences between 2030 A1B/B1 and baseline values for several variables. Because data in the future atmosphere are not available, it is not possible to quantify the uncertainty of the results. However, the comparisons with data (Figures 1 and 3 and previous papers) give an indication of the accuracy of the model with respect to some parameters.

[55] Aerosol optical depth (AOD) decreased in the U.S., Europe, and Sahel and increased in much of the rest of the world in the A1B and B1 scenarios relative to the baseline scenario (Figure 4). AOD decreases in the U.S. and Europe were due primarily to decreases in sulfate (Figure 4), BC (Figure 4), POM, and liquid water. Decreases in the Sahel were due to increases in precipitation there (Figure 6). AOD increased in much of the rest of the world because BC, POM, SOM, sulfate, nitrate, and ammonium increased elsewhere in both scenarios (e.g., Figure 4). In the global average, AOD increased by about 1.4% in the A1B scenario and decreased by about 4.9% in the B1 scenario (Table 6), paralleling the greater aerosol emissions in the A1B relative to the B1 scenario.

[56] In the A1B scenario, high anthropogenic aerosol and precursor gas emission rates were offset only in part by natural soil dust emission decreases to cause a net increase aerosol column mass (Table 6). In the B1 scenario, anthropogenic aerosol emission increases were lower than in the A1B scenario and soil dust emission decreases were greater than in the A1B scenario, resulting in a net reduction in aerosol column mass.

[57] The aerosol decrease in Western Europe and the eastern U.S. in particular reduced cloud optical depths (CODs) there in both scenarios (Figure 5). In South America and southeast Asia, aerosol increases increased CODs (Figure 5). Globally, CODs and cloud fractions increased by 3.2% and 0.15%, respectively, in the A1B scenario and decreased by 8.2% and 0.37%, respectively, in the B1 scenario (Table 6). COD/cloud fraction changes correlated spatially with AOD changes. In locations where COD decreased (increased), surface solar radiation increased (decreased) (Figure 5) and surface thermal-IR radiation decreased (increased). Globally, surface solar radiation decreased by 0.22% in the A1B scenario and increased by 0.64% in the B1 scenario, reflecting the fact that AOD and COD decreases were greater in the B1 scenario than in the A1B scenario (Table 6).

[58] Global surface air temperatures increased in both scenarios, but more in the "cleaner" B1 scenario (+0.16 K versus +0.007K) (Figure 6) despite lower CO_2 and CH_4 emissions in the B1 scenario. This occurred because aerosol emissions increased more in the A1B than in the B1 scenario, increasing aerosol and cloud optical depths in the A1B relative to the B1 scenario, masking more warming in the A1B scenario.

[59] Global precipitation decreased in the A1B scenario by about 0.13% and increased in the B1 scenario by about 0.08% (Table 6). The locations of precipitation increases and decreases in both scenarios correlate very well spatially with AOD decreases and increases, respectively (Figure 4) and temperature increases and decreases, respectively (Figure 6). For example, precipitation increased over North America and Europe (Figure 6), where temperatures increased and AODs decreased in both scenarios, and decreased noticeably over South America, where AODs increased in both scenarios.

[60] *Jacobson and Kaufman* [2006] found that aerosol particles alone reduce near-surface wind speeds by stabilizing the air, reducing the vertical transport of horizontal momentum. In the A1B scenario here, AOD increased (Table 6, Figure 4), stabilizing the air over land and the ocean (Table 6), reducing shearing stress (Table 6), decreasing wind speed on average (Table 6, Figure 6). In the B1 scenario, AOD decreased (Table 6, Figure 4) increasing near-surface wind speeds (Table 6, Figure 6).

[61] Warmer temperatures over land in both scenarios increased evaporation over land, decreasing soil moisture (Table 6). Cloud liquid increased in the A1B scenario (Table 6) due to lower precipitation (Table 6) in that scenario. Cloud liquid decreased in the B1 scenario, and this is correlated with greater precipitation in that scenario.

[62] In both scenarios, surface ozone increased (Table 6, Figure 7). Ozone increases were greater in the A1B scenario, which had larger emissions of ozone precursor organic gases and NO_x (Table 2) than in the B1 scenario. Ozone increases could have been larger in the A1B scenario, except that higher AODs and CODs in that scenario decreased UV radiation more than in the B1 scenario (Table 6). In the B1 scenario, the ozone increases were due to increases in organic gases and UV radiation (due to a net decrease in AOD and CODs) (Table 6), tempered by lower NO_x emissions (Table 2).

[63] PAN increased in the A1B scenario due to much higher precursor emissions in that scenario, but hardly changed in the B1 scenario (Table 6, Figure 7) due to moderate increases in organic gas precursors in that scenario offset by warmer temperatures, which enhance PAN thermal dissociation. CO's emissions (Table 2) and mixing ratio
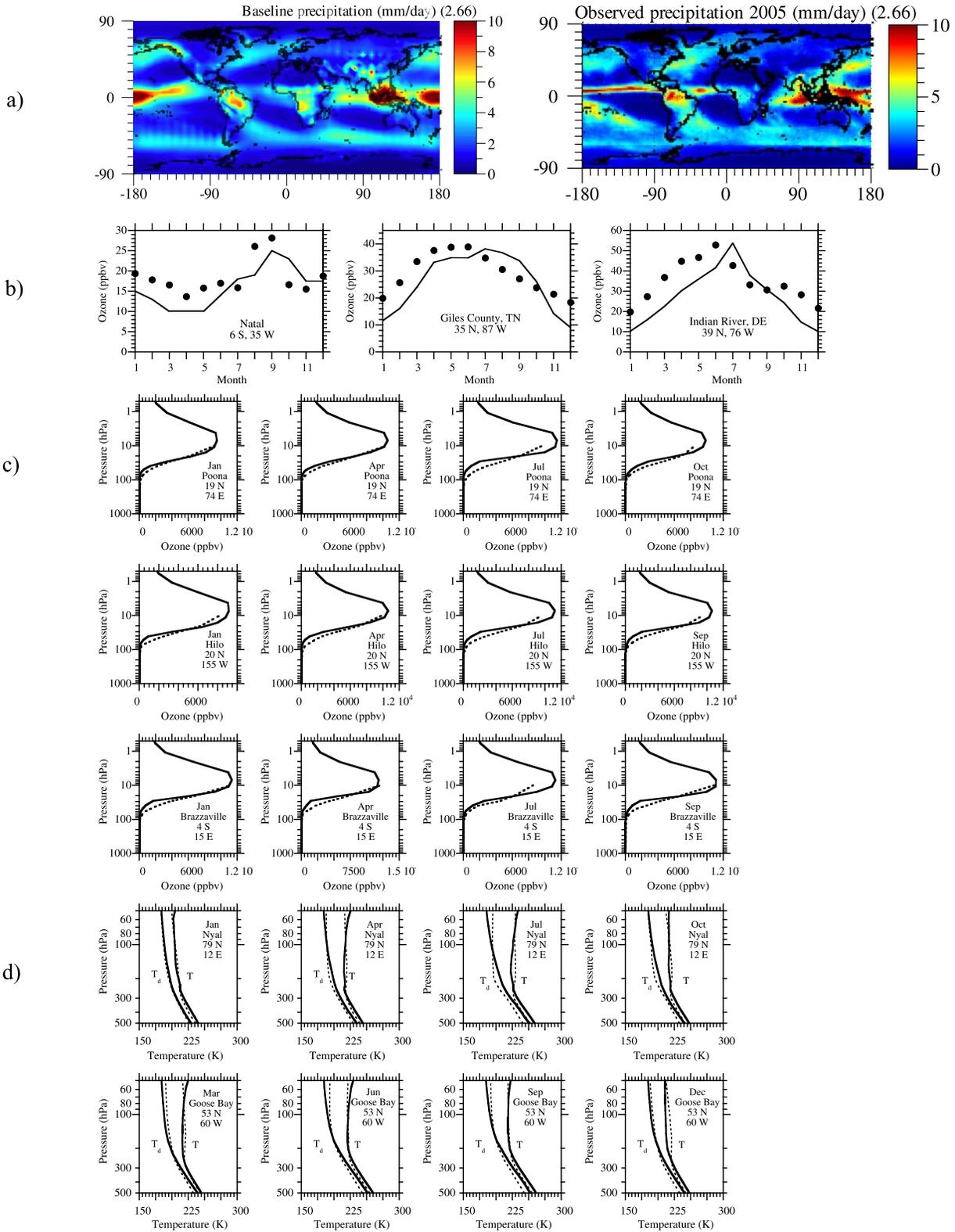
Figure 3. (a) Simulation-averaged modeled baseline (4° × 5° resolution) versus 2005 observed [*Huffman et al.*, 2001] precipitation. (b) Modeled baseline (solid lines) versus observed (solid dots [*Logan*, 1999a]) monthly averaged ozone. (c) Modeled baseline (solid lines) versus observed (dashed lines [*Logan*, 1999b]) monthly averaged vertical ozone profiles. (d) Modeled baseline (solid lines) versus observed (dashed lines [*FSL*, 2008]) monthly averaged vertical temperature and dew point profiles.

Table 6. Modeled Globally Averaged and Simulation-Averaged 2000 Baseline Values and Percentage Differences Between the 2030 A1B/B1 and the Baseline Values[a]

Species	2000 Baseline	2030 A1B − Base (% change)	2030 B1 − Base (% change)
Aerosol optical depth	0.200	+1.4	−4.9
Column aerosol mass (mg/m^2)	178	+1.8	−4.0
Column aerosol number (no./cm^2)	1.62×10^9	−7.1	−3.1
Cloud optical depth	4.90	+3.2	−8.2
Cloud absorption optical depth	0.000049	+7.2	−24
Cloud liquid mass (kg/m^2)	0.0128	+3.6	−0.27
Activated CCN (no./cm^3)	2.63	−2.0	−24
Cloud ice (kg/m^2)	0.0048	−3.1	−0.83
Activated IDN (no./cm^3)	0.051	−8.3	−5.0
Cloud fraction	0.59	+0.15	−0.37
Surface thermal-IR irradiance (W/m^2)	−71.4	−0.004	+0.66
Surface solar irradiance (W/m^2)	171	−0.22	+0.64
Surface UV irradiance (W/m^2)	9.76	−0.27	+1.0
38-m air temperature (K)	287.8	+0.0023	+0.057
Ground temperature (K)	288.3	+0.0007	+0.052
TKE (m^2/s^2)	0.117	+1.1	−2.8
Shear stress (kg/m/s)	0.121	−0.41	−0.25
38-m wind speed (m/s)	5.82	−0.23	+0.16
Near-surface RH (fraction)	0.737	−0.28	−0.25
Precipitation (mm/day)	2.66	−0.13	+0.076
Soil moisture (m^3/m^3, land only)	0.229	−0.091	−0.20
Sea ice depth (m)	0.074	−0.88	−0.025
Snow depth (m)	3.79	−0.019	−0.037
Surface albedo	0.174	−0.054	−0.24
Ocean pH	7.87	−0.055	−0.025
Near-surface aerosol SSA	0.946	+0.077	+0.20
Near-surface NO (ppbv)	0.23	+81	−21.1
Near-surface NO$_2$ (ppbv)	0.43	+51	−19.7
Near-surface HNO$_3$ (ppbv)	0.034	+76	−12.1
Near-surface OH (pptv)	0.000019	−3.8	−7.9
Near-surface O$_3$ (ppbv)	15.8	+14	+3.9
Near-surface PAN (ppbv)	0.46	+23	−8.9
Near-surface CO (ppbv)	146	+12	−0.28
Near-surface CO$_2$ (ppmv)	396	+1.5	+0.75
Near-surface CH$_4$ (ppmv)	1.91	+0.71	+0.09
Near-surface HCHO (ppbv)	0.87	+14	+5.2
Near-surface higher aldehydes (ppbv)	1.0	+23	+33
Near-surface benzene (ppbv)	0.19	−3.7	−19
Near-surface toluene (ppbv)	0.076	+14	+5.6
Near-surface isoprene (ppbv)	0.47	−5.7	+3.7
Near-surf. monoterpenes (ppbv)	0.069	−6.0	+2.0
Near-surface SO$_2$ (ppbv)	0.36	+40	−20
Near-surface NH$_3$ (ppbv)	0.62	−15	−5.0
Column NO (mg/m^2)	0.39	+16	−5.2
Column NO$_2$ (mg/m^2)	1.05	+15	−7.1
Column HNO$_3$ (mg/m^2)	13.7	−0.27	−0.47
Column OH (mg/m^2)	0.0069	−0.44	+0.18
Column H$_2$O (kg/m^2)	29.4	−0.71	+0.85
Column O$_3$ (mg/m^2)	6400	−0.005	−0.02
Column PAN (mg/m^2)	21.8	+23	+0.85
Column CO (mg/m^2)	1260	+12	+4.9
Column CO$_2$ (g/m^2)	6050	+1.18	+0.59
Column CH$_4$ (g/m^2)	10.1	+0.65	+0.14
Column HCHO (mg/m^2)	3.3	+14	+8.1
Column higher aldehydes (mg/m^2)	7.2	+48	+38
Column benzene (mg/m^2)	2.1	−0.79	−16
Column toluene (mg/m^2)	0.42	+17.9	+18
Column isoprene (mg/m^2)	1.1	−8.9	+3.5
Column monoterpenes (mg/m^2)	0.12	−4.5	+3.1
Column SO$_2$ (mg/m^2)	1.1	+16.6	−5.6
Column NH$_3$ (mg/m^2)	0.21	−41.7	−14
Near-surface PM$_{2.5}$ (μg/m^3)	44.4	+1.6	−1.8
Column BC (mg/m^2)	0.20	+12.2	−16
Column POM (mg/m^2)	1.8	−10.4	−18
Column SOM (mg/m^2)	5.7	−1.7	−15
Column aer-H$_2$O(aq) (mg/m^2)	43	+0.37	−2.4
Column S(VI) (mg/m^2)	4.1	+15.3	−1.5
Column NO$_3^-$ (mg/m^2)	1.1	+6.0	−3.5
Column Cl$^-$ (mg/m^2)	1.4	−4.1	−0.91
Column H$^+$ (mg/m^2)	0.044	+11	+0.39
Column NH$_4^+$ (mg/m^2)	0.31	+7.1	−9.2
Column NH$_4$NO$_3$(s) (mg/m^2)	0.94	+11	−2.3

Table 6. (continued)

Species	2000 Baseline	2030 A1B − Base (% change)	2030 B1 − Base (% change)
Column $(NH4)_2SO_4(s)$	0.41	−19	−4.4
Column Na^+ (mg/m^2)	1.4	−1.6	−1.1
Column soil dust (mg/m^2)	120	+2.0	−4.3
Column pollen/spores/bacteria (mg/m^2)	0.61	+2.3	+1.3

[a]Divide mg/m^2 by 1.9637 to obtain Tg.

(Table 6) increased in the A1B scenario and decreased slightly in the B1 scenario. Formaldehyde and acetaldehyde emissions and mixing ratios increased significantly in both scenarios.

6. Effects on Natural Emissions

[64] Climate changes in 2030 fed back to the natural emissions of particles and gases. Lightning NO, NO_2, HONO, HNO_3, N_2O, CO, HO_2, and H_2O_2 decreased in the A1B and B1 scenarios (Table 4) due to decreased cloud ice and liquid number in both scenarios (Table 6). Figures 1c and 1d show that lightning NO decreased at all altitudes in the A1B scenario and all altitudes except above 250 hPa in the B1 scenario. At higher altitudes in the B1 scenario, cloud ice increased because greater tropospheric warming in the B1 scenario caused a greater dropoff in temperature in the upper troposphere, increasing upper-tropospheric instability, allowing ice clouds to penetrate higher. The warming in the A1B scenario was weaker, particularly in the upper troposphere, than in the B1 scenario, thus no upper-tropospheric instability occurred in the A1B scenario.

[65] Although anthropogenic aerosol particle emissions increased in the A1B and decreased in the B1 scenario, natural soil dust emissions, the largest among natural particle components, decreased in both scenarios as a result of climate change (Table 4), causing a net reduction in total aerosol column number in both scenarios (Table 6). At the same time, warmer tropospheric temperatures in both scenarios decreased cloud ice mass, shrinking or melting ice crystals, increasing cloud liquid.

[66] The reduction in cloud ice number decreased the number of collisions, thus bounceoffs, between ice crystals, reducing charge separation and the number of lightning strokes. Since smaller ice crystals coalesce more efficiently, the shrinking of ice crystals in some cases also reduced the number of bounceoffs. Since ice crystals carry more charge than liquid drops (section 3.2), changes in ice crystal number and size were more important than changes in cloud liquid number and size.

[67] Previous studies, none of which considered the rebound mechanism of lightning formation or the larger charge on ice than liquid drops, found little change [*Stevenson et al.*, 2005] or slight increases [*Unger et al.*, 2006; *Liao et al.*, 2006] in NO_x from lightning due to future warming. In some such cases, the lightning flash rate was a function primarily of cloud top height so changes in ice crystal or cloud liquid number due to future climate change did not feed back directly to the flash rate.

[68] Soil NO emissions, which depended on temperature and canopy wind speed, increased by ∼0.2% in the A1B scenario and ∼1.6% in the B1 scenario due to a greater

land temperature increase in the B1 scenario (Figure 6). This increase is consistent with previous studies [e.g., *Liao et al.*, 2006]. Soil N_2O, H_2, and CH_4 emissions increased proportionally to soil NO emissions (Table 4) as explained in section 3.3. Soil H_2S, DMS, OCS, and CS_2 emissions, which were primarily a function of temperature, also increased more in the B1 scenario than in the A1B scenario (Table 4).

[69] Isoprene emissions from vegetation depended on temperature and PAR. Monoterpene and other VOC emissions depended on temperature only. Isoprene and other VOC emissions increased by ∼1% in the A1B scenario but by ∼4−5% in the B1 scenario due to smaller temperature increases and less sunlight in the A1B scenario than in the B1 scenario (Table 6). The increases in biogenic organic gas emissions in a future climate are consistent with results from other studies [e.g., *Sanderson et al.*, 2003; *Brasseur et al.*, 2006; *Liao et al.*, 2006]. Although isoprene and monoterpene emissions increased in both scenarios, their ambient levels decreased in the A1B scenario due to reaction with the enhanced ozone in that scenario (Table 6, Figure 7). Ozone increased by a lesser amount in the B1 scenario, resulting in a net increase in ambient isoprene and monoterpenes.

[70] Ocean DMS, N_2O, H_2, CH_4, sea spray, and ocean bacteria emissions depended primarily on wind speed (which decreased in the A1B but increased in the B1 scenario over the ocean; Figure 6), but also on temperature (which increased globally but decreased due to enhanced cloud optical depth in the southern ocean; Figures 5 and 6), and sea ice cover (which decreased in both scenarios). The changes in average ocean wind speed controlled sea spray and ocean bacteria emissions, decreasing them in the A1B scenario and increasing them in the B1 scenario. The B1 scenario result is consistent in direction with the reduction in sea spray between 2000 and 2100 by *Liao et al.* [2006]. Since DMS, N_2O, H_2, and CH_4 are emitted only in the presence of biological activity, their emissions depended more on regional wind speeds. Such wind speeds decreased on average in the regions of phytoplankton growth (Figure 6).

[71] Land bacteria and pollen emissions depended on turbulent kinetic energy (TKE) and snow cover. TKE increased by ∼1% in the A1B scenario and decreased by ∼3% in the B1 scenario (Table 6), causing pollen to increase in the A1B scenario and decrease in the B1 scenario. Land bacteria increased in both scenarios since the decrease in snow cover in both scenarios (Table 6) increased land bacteria emissions in the A1B scenario greater than the reduction in wind speed decreased such emissions. Spore emissions depended on TKE and inversely on snow cover and relative humidity (both of which decreased in both scenarios). Because snow and RH decreases, spore emissions increased in both scenarios.
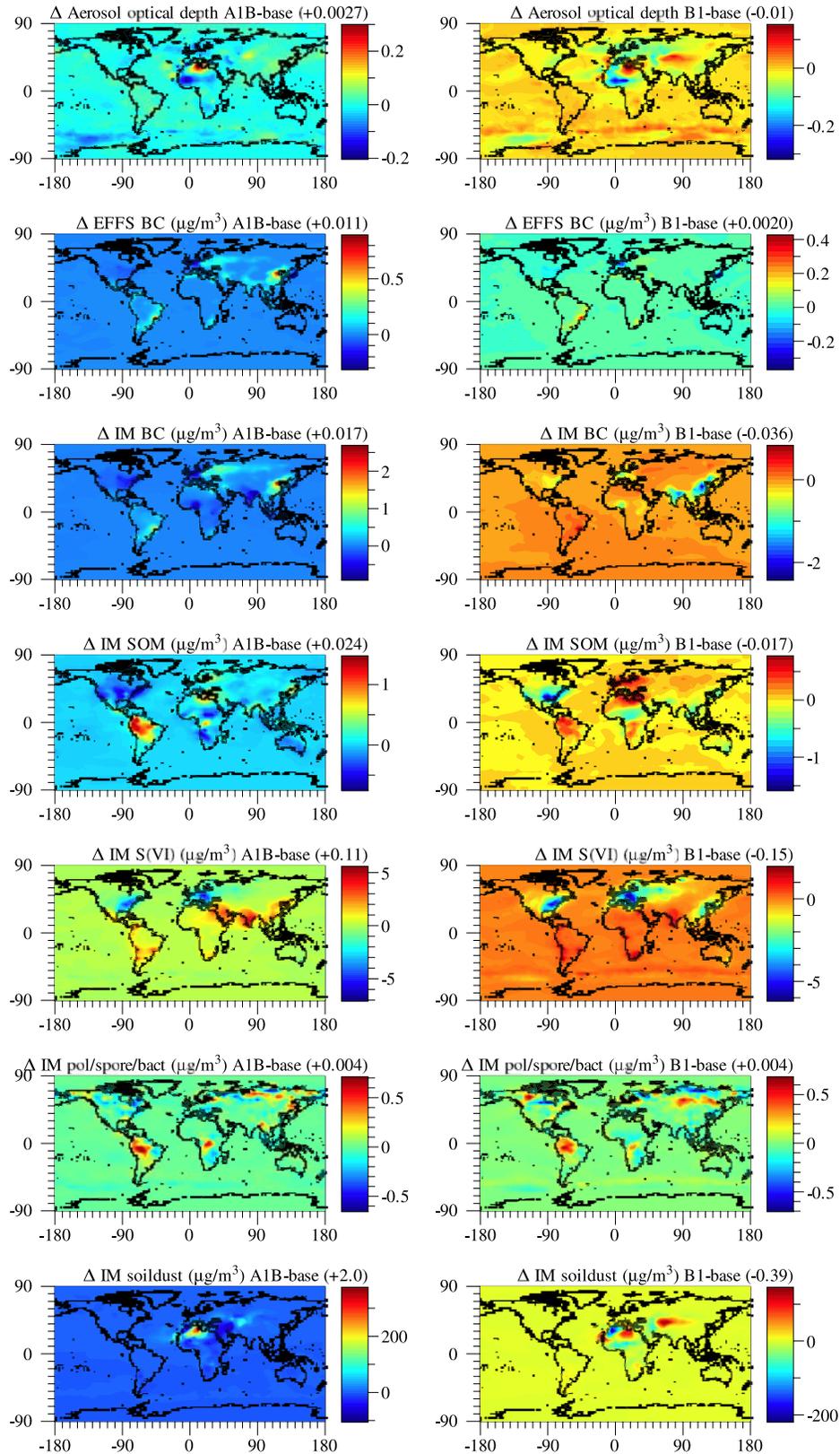
Figure 4. Modeled simulation-averaged differences in several aerosol parameters when a 2030 (A1B and B1) emission scenario was used versus when a near-present (base) emission scenario was used. Mixing ratios and concentrations are near-surface values. IM, internally mixed; EFFS, emitted fossil fuel soot (e.g., Table 1).
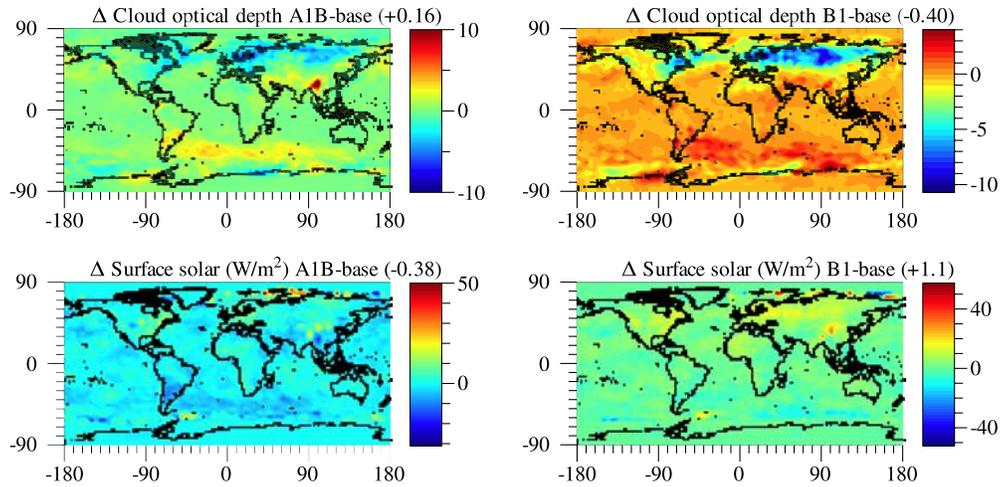
Figure 5. Same as Figure 4, but for cloud parameters.

The sum of ambient column pollen, spores, and bacteria increased by about 2% in the A1B scenario and by about 1.3% in the B1 scenario.

[72] Soil dust emissions depended on wind speed, temperature, soil moisture, and snow cover. Soil dust emissions decreased by ∼0.2% in the A1B and by ∼4% in the B1 scenario. Ambient soil dust increased by ∼2% in the A1B scenario due to slightly lower land precipitation, particularly over the Sahara, in that scenario (Figure 7), whereas it decreased by ∼4% in the B1 scenario, consistent with its emission change.

[73] Photosynthesis depended on the temperature, the relative humidity, and PAR. Plant respiration depended on

temperature, and soil bacteria respiration depended on temperature and soil moisture. Carbon uptake by plants due to photosynthesis (gross primary production, GPP) in the base case was 118 Pg C/a, close to the *IPCC* [2001] estimate of 120 Pg C/a. The net primary production (NPP) (GPP – cellular respiration) of carbon in the base case was 53.4 Pg C/a, within the range of 44.4–66.3 Pg C/a found from an intercomparison among 16 global models [*Cramer et al.*, 1999, Table 5]. GPP and plant respiration increased in both scenarios (Table 4) due primarily to temperature and PAR increases in the B1 scenario and temperature increases in the A1B scenario (Figure 6). Bacteria respiration in soil decreased in the A1B scenario due to lower soil moisture in
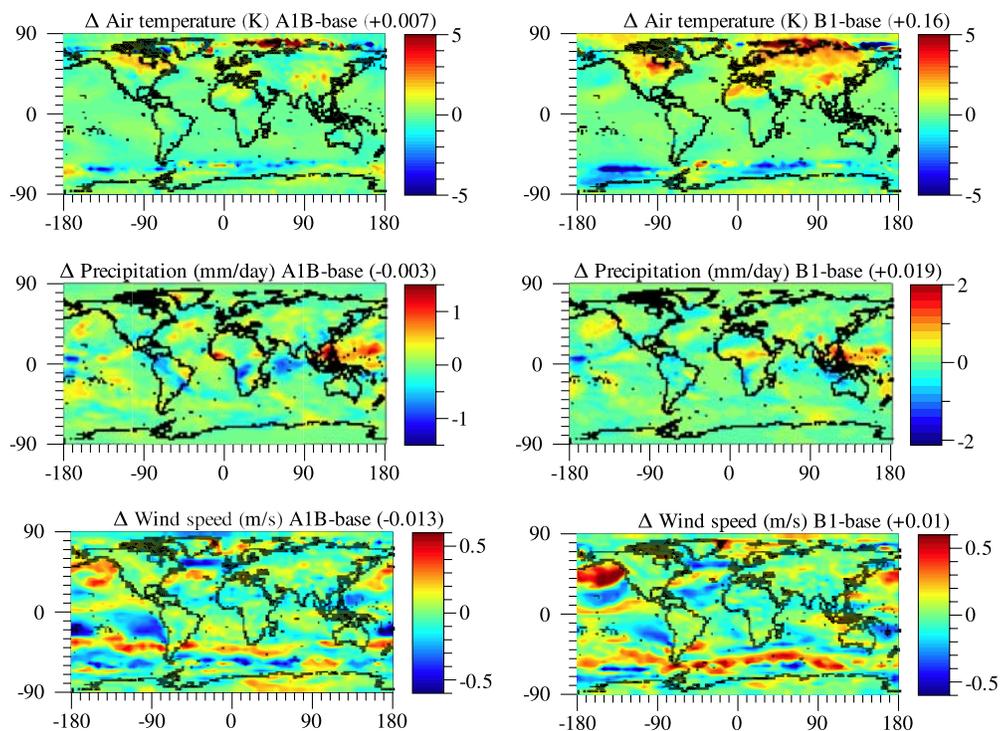
Figure 6. Same as Figure 4, but for radiative parameters.
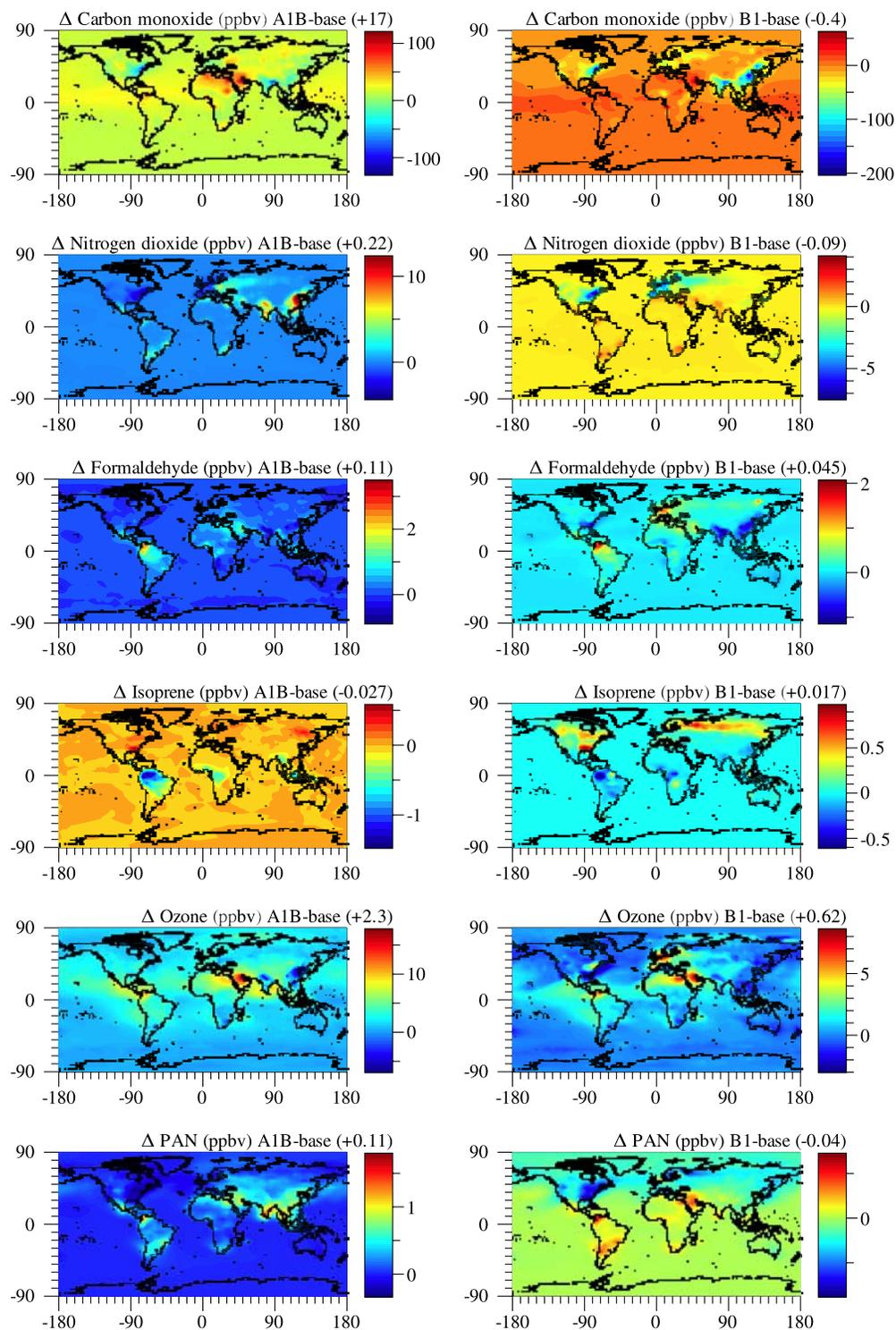
Figure 7. Same as Figure 4, but for gas parameters.

that scenario. Soil moisture decreased more in the B1 scenario, but temperatures were higher than in the A1B scenario, causing a net respiration increase in the B1 scenario.

[74] Global methanol emissions from plant growth and decay in the base case were 50 Tg C/a, which compares with 56.6 (39.9–75) Tg C/a from data by *Jacob et al.* [2005]. Such emissions increased by ~2% in both future

scenarios relatively proportional to increases in NPP plus soil respiration.

7. Conclusions

[75] Speciated emission factors as a function of world region and emission sector were developed following IPCC SRES A1B and B1 trajectories and applied to a recent-year

emission inventory to produce anthropogenic gas and particle inventories for 2030. The baseline and future inventories were then used in transient climate simulations to examine the potential effects of emission changes on climate and air quality, and how changes in future climate might affect natural emissions of aerosol particles and gases. Natural emissions affected by climate included NO, NO_2, HONO, HNO_3, N_2O, CO, HO_2, and H_2O_2 from lightning; sea spray and its constituents; ocean bacteria, DMS, N_2O, H_2, and CH_4; soil dust; isoprene, monoterpenes, methanol, and other organics from vegetation; NO, N_2O, H_2, CH_4, H_2S, DMS, OCS, and CS_2 from soils; pollen; spores; land bacteria; and carbon dioxide from the soils, leaves, and the ocean.

[76] Under the A1B scenario, global emissions of greenhouse gases, smog-precursor gases, and aerosol particles were higher than today; under the B1 scenario, emissions of greenhouse and most organic gases were higher than today but emissions of other gases and aerosol particle were lower than today, with significant regional variation. Although the B1 scenario was "cleaner" than the A1B scenario, the B1 scenario enhanced global warming more because greater warming in the A1B scenario was masked by increases in reflective aerosol particles in that scenario. This result implies that neither scenario is entirely beneficial. One slows warming but increases particle loadings, whereas the other reduces particles but speeds up warming. The ideal policy then is to reduce warming gases and both warming and cooling particles simultaneously.

[77] Globally averaged near-surface ozone increased by ∼14% in the A1B scenario and ∼4% in the B1 scenario due to emission increases of some organics (e.g., formaldehyde, higher aldehydes) in both scenarios, an increase in NO_x in the A1B scenario, and an increase in UV radiation in the B1 scenario. Near-surface PAN increased by ∼23% in the A1B scenario but decreased by ∼9% in the higher-temperature B1 scenario. Near-surface $PM_{2.5}$ mass increased by ∼2% in the A1B scenario (due to greater anthropogenic emissions than in the baseline case) and decreased by ∼2% in the B1 scenario (due to lower emissions).

[78] A new method of calculating the lightning flash rate was developed. It treated size-resolved collisional bounce-offs among ice, graupel, and liquid. Because ice crystals carry more charge than do liquid drops, the reduction in ice crystal concentration due to tropospheric warming reduced lightning and its gas emissions by ∼3% in the B1 scenario and ∼12% in the A1B scenario. New climate-dependent equations for calculating emissions of pollen, spores, and land/ocean bacteria were also developed and used.

[79] The emission rates of wind-driven sea spray and ocean bacteria decreased by ∼0.4% in the A1B scenario due to slower ocean winds in that scenario caused by higher aerosol and cloud optical depths, which enhanced stability, reducing shearing stress. Lower AODs in the B1 scenario had the opposite effect, increasing ocean sea spray by ∼0.7%. Isoprene and monoterpene emissions increased by ∼1% in the A1B scenario and 4–5% in the B1 scenario from enhanced precursor gases. Ambient isoprene decreased in the A1B scenario due to higher ozone. Net primary production of carbon and gas emissions from soils increased by ∼2% in both scenarios. Results here are subject to uncertainties arising from model grid resolution,

simulation time, numerical treatments, physical processes treated and emission data.

References

Andreae, M. O., and P. Merlet (2001), Emission of trace gases and aerosols from biomass burning, *Global Biogeochem. Cycles*, *15*, 955–966.

Andres, R. J., and A. D. Kasgnoc (1998), A time-averaged inventory of subaerial volcanic sulfur emissions, *J. Geophys. Res.*, *103*, 25,251–25,261.

Aw, J., and M. J. Kleeman (2003), Evaluating the first-order effect of intraannual temperature variability on urban air pollution, *J. Geophys. Res.*, *108*(D12), 4365, doi:10.1029/2002JD002688.

Aylor, D. E., and J.-Y. Parlange (1975), Ventilation required to entrain small particles from leaves, *Plant Physiol.*, *56*, 97–99.

Bauer, H., H. Giebl, R. Hitzenberger, A. Kasper-Giebl, G. Reischl, F. Zibuschka, and H. Puxbaum (2003), Airborne bacteria as cloud condensation nuclei, *J. Geophys. Res.*, *108*(D21), 4658, doi:10.1029/2003JD003545.

Beard, K. V., and H. T. Ochs III (1984), Collection and coalescence efficiencies for accretion, *J. Geophys. Res.*, *89*, 7165–7169.

Bernacchi, C. J., C. Pimentel, and S. P. Long (2003), In vivo temperature response functions of parameters required to model RuBP-limited photosynthesis, *Plant, Cell Environ.*, *26*, 1419–1430.

Bhetanabhotla, M. N., B. A. Crowell, A. Coucouvinos, R. D. Hill, and R. G. Ringer (1985), Simulation of trace species production by lightning and corona discharge in moist air, *Atmos. Environ.*, *19*, 1391–1397.

Bond, T. C., D. G. Streets, K. F. Yarber, S. M. Nelson, J.-H. Woo, and Z. Klimont (2004), Development of a global black carbon inventory, *J. Geophys. Res.*, *109*, D14203, doi:10.1029/2003JD003697.

Bouwman, A. F., K. W. Van der Hoek, and J. G. J. Olivier (1995), Uncertainties in the global source distribution of nitrous oxide, *J. Geophys. Res.*, *100*, 2785–2800.

Bouwman, A. F., D. S. Lee, W. A. H. Asman, F. J. Dentener, K. W. van der Hoek, and J. G. J. Olivier (1997), A global high-resolution emission inventory for ammonia, *Global Biogeochem. Cycles*, *11*, 561–587.

Bovallius, A., B. Bucht, R. Roffey, and P. Anas (1978), Three-year investigation of the natural airborne bacterial flora at four localities in Sweden, *Appl. Environ. Microbiol.*, *35*, 847–852.

Brasseur, G. P., J. T. Kiehl, J.-F. Mueller, T. Schneider, C. Granier, X. X. Tie, and D. Hauglustaine (1998), Past and future changes in global tropospheric ozone: Impact on radiative forcing, *Geophys. Res. Lett.*, *25*, 3807–3810.

Brasseur, G. P., M. Schultz, C. Granier, M. Saunois, T. Diehl, M. Botzet, and E. Roeckner (2006), Impact of climate change on the future chemical composition of the global troposphere, *J. Clim.*, *19*, 3932–3951.

Burch, M., and E. Levetin (2002), Effects of meteorological conditions on spore plumes, *J. Int. Biometeorol.*, *46*, 107–117.

Carisse, O., and V. Philion (2002), Meteorological factors affecting periodicity and concentration of airborne spores of *Bremia lactucae*, *Can. J. Plant Pathol.*, *24*, 184–193.

Christian, H. J., et al. (2003), Global frequency and distribution of lightning as observed from space by the optical transient detector, *J. Geophys. Res.*, *108*(D1), 4005, doi:10.1029/2002JD002347.

Clarke, A. D., S. R. Owens, and J. Zhou (2006), An ultrafine sea-salt flux from breaking waves: Implications for cloud condensation nuclei in the remote marine atmosphere, *J. Geophys. Res.*, *111*, D06202, doi:10.1029/2005JD006565.

Collatz, G. J., J. T. Ball, C. Grivet, and J. A. Berry (1991), Physiological and environmental regulation of stomatal conductance, photosynthesis, and transpiration: A model that includes a laminar boundary layer, *Agric. For. Meteorol.*, *54*, 107–136.

Collatz, G. J., M. Ribas-Carbo, and J. A. Berry (1992), Coupled photosynthesis-stomatal conductance model for leaves of C4 plants, *Aust. J. Plant Physiol.*, *19*, 519–538.

Coppens, F., R. Berton, A. Bondiou-Clergerie, and I. Gallimberti (1997), Theoretical estimate of NO_x production in lightning corona, *J. Geophys. Res.*, *103*, 10,769–10,785.

Corbett, J. J., and H. W. Koehler (2003), Updated emissions from ocean shipping, *J. Geophys. Res.*, *108*(D20), 4650, doi:10.1029/2003JD003751.

Corbett, J. J., P. S. Fischbeck, and S. N. Pandis (1999), Global nitrogen and sulfur emissions inventories for oceangoing ships, *J. Geophys. Res.*, *104*, 3457–3470.

Cramer, W., D. W. Kicklighter, A. Bondeau, B. Moore III, G. Churkina, B. Nemry, A. Ruimy, and A. L. Schloss (1999), Comparing global models of terrestrial net primary productivity: Overview and key results, *Global Change Biol.*, *5*(Suppl. 1), 1–15.

Eversmeyer, M. G., C. L. Kramer, and J. R. Burleigh (1971), Vertical spore concentrations of three wheat pathogens above a wheat field, *Phytopathology*, *63*, 211–218.

Farquhar, G. D., S. von Caemmerer, and J. A. Berry (1980), A biochemical model of photosynthetic CO_2 assimilation in leaves of C_3 species, *Planta*, *149*, 78–90.

Food and Agricultural Organization (FAO) (1995), *Soil Map of the World*, Land and Water Devt. Div., FAO, Rome, Italy.

Forecast Systems Laboratory (FSL) (2008), Recent worldwide RAOB observations [CD-ROM], available at http://www.fsl.noaa.gov/data/onlinedb.html.

Fuglestvedt, J. S., J. E. Jonson, W.-C. Wang, and I. S. A. Isaksen (1995), Responses in tropospheric chemistry to changes in UV fluxes, temperatures and water vapour densities, in *Atmospheric Ozone as a Climate Gas*, edited by W.-C. Wang and I. S. A. Isaksen, *NATO ASI Ser.*, Springer, Berlin.

Futyan, J. M., and A. D. Del Genio (2007), Relationships between lightning and properties of convective cloud clusters, *Geophys. Res. Lett.*, *34*, L15705, doi:10.1029/2007GL030227.

Giglio, L., G. R. van der Werf, J. T. Randerson, G. J. Collatz, and P. Kasibhatla (2006), Global estimation of burned area using MODIS active fire observations, *Atmos. Chem. Phys.*, *6*, 957–974.

Global Hydrology and Climate Center (GHCC) Lightning Team (2008), LIS/OTD Gridded dataset, available at http://thunder.nsstc.nasa.gov/data/index.html.

Grewe, V., M. Dameris, R. Hein, R. Sausn, and B. Steil (2001), Future changes of the atmospheric composition and the impact of climate change, *Tellus, Ser. B.*, *53*, 103–121.

Guenther, A., et al. (1995), A global model of natural volatile organic compound emissions, *J. Geophys. Res.*, *100*, 8873–8892.

Hameed, S., and R. Cess (1983), Impact of global warming on biospheric sources of methane and its climatic consequences, *Tellus, Ser. B.*, *35B*, 1–7.

Hauglustaine, D., L. Emmons, M. Newchurch, G. Brasseur, T. Takao, K. Matsubara, J. Johnson, B. Ridley, J. Stith, and J. Dye (2001), On the role of lightning NO_x in the formation of tropospheric ozone plumes: A global model perspective, *J. Atmos. Chem.*, *38*, 277–294.

Howard, D. M., and P. J. A. Howard (1993), Relationships between CO_2 evolution, moisture content, and temperature for a range of soil types, *Soil Biol. Biochem.*, *25*, 1537–1546.

Huffman, G. J., R. F. Adler, M. M. Morrissey, S. Curtis, R. Joyce, B. McGavock, and J. Susskind (2001), Global precipitation at one-degree daily resolution from multi-satellite observations, *J. Hydrometeorol.*, *2*, 36–50.

Intergovernmental Panel on Climate Change (IPCC) (2001), *Third Assessment Report, Climate Change 2001: The Scientific Basis*, edited by J. T. Houghton et al., chap. 4, Cambridge Univ. Press, New York.

Jacob, D. J., B. D. Field, Q. Li, D. R. Blake, J. de Gouw, C. Warneke, A. Hansel, A. Wisthaler, H. B. Singh, and A. Guenther (2005), Global budget of methanol: Constraints from atmospheric observations, *J. Geophys. Res.*, *110*, D08303, doi:10.1029/2004JD005172.

Jacobson, M. Z. (1997), Development and application of a new air pollution modeling system: part III. Aerosol-phase simulations, *Atmos. Environ.*, *31A*, 587–608.

Jacobson, M. Z. (2001a), GATOR-GCMM: A global through urban scale air pollution and weather forecast model: 1. Model design and treatment of subgrid soil, vegetation, roads, rooftops, water, sea ice, and snow, *J. Geophys. Res.*, *106*, 5385–5402.

Jacobson, M. Z. (2001b), GATOR-GCMM: 2. A study of day- and night-time ozone layers aloft, ozone in national parks, and weather during the SARMAP Field Campaign, *J. Geophys. Res.*, *106*, 5403–5420.

Jacobson, M. Z. (2002a), Analysis of aerosol interactions with numerical techniques for solving coagulation, nucleation, condensation, dissolution, and reversible chemistry among multiple size distributions, *J. Geophys. Res.*, *107*(D19), 4366, doi:10.1029/2001JD002044.

Jacobson, M. Z. (2002b), Control of fossil-fuel particulate black carbon plus organic matter, possibly the most effective method of slowing global warming, *J. Geophys. Res.*, *107*(D19), 4410, doi:10.1029/2001JD001376.

Jacobson, M. Z. (2003), Development of mixed-phase clouds from multiple aerosol size distributions and the effect of the clouds on aerosol removal, *J. Geophys. Res.*, *108*(D8), 4245, doi:10.1029/2002JD002691.

Jacobson, M. Z. (2004), The climate response of fossil-fuel and biofuel soot, accounting for soot's feedback to snow and sea ice albedo and emissivity, *J. Geophys. Res.*, *109*, D21201, doi:10.1029/2004JD004945.

Jacobson, M. Z. (2005a), A refined method of parameterizing absorption coefficients among multiple gases simultaneously from line-by-line data, *J. Atmos. Sci.*, *62*, 506–517.

Jacobson, M. Z. (2005b), *Fundamentals of Atmospheric Modeling*, 2nd ed., 813 pp., Cambridge Univ. Press, New York.

Jacobson, M. Z. (2005c), Studying ocean acidification with conservative, stable numerical schemes for nonequilibrium air-ocean exchange and ocean equilibrium chemistry, *J. Geophys. Res.*, *110*, D07302, doi:10.1029/2004JD005220.

Jacobson, M. Z. (2006), Effects of absorption by soot inclusions within clouds and precipitation on global climate, *J. Phys. Chem.*, *110*, 6860–6873.

Jacobson, M. Z. (2008), On the causal link between carbon dioxide and air pollution mortality, *Geophys. Res. Lett.*, *35*, L03809, doi:10.1029/2007GL031101.

Jacobson, M. Z., and Y. J. Kaufman (2006), Wind reduction by aerosol particles, *Geophys. Res. Lett.*, *33*, L24814, doi:10.1029/2006GL027838.

Jacobson, M. Z., Y. J. Kaufmann, and Y. Rudich (2007), Examining feedbacks of aerosols to urban climate with a model that treats 3-D clouds with aerosol inclusions, *J. Geophys. Res.*, *112*, D24205, doi:10.1029/2007JD008922.

Johnson, C. E., W. J. Collins, D. S. Stevenson, and R. G. Derwent (1999), The relative roles of climate and emissions changes on future oxidant concentrations, *J. Geophys. Res.*, *104*, 18,631–18,645.

Johnson, C. E., D. S. Stevenson, W. J. Collins, and R. G. Derwent (2001), Role of climate feedback on methane and ozone studied with a coupled ocean-atmosphere chemistry model, *Geophys. Res. Lett.*, *28*, 1723–1726.

Karl, D. M., L. Beversdorf, K. M. Bjorkman, M. J. Church, A. Martinez, and E. F. Delong (2008), Aerobic production of methane in the sea, *Nat. Geosci.*, *1*, 473–478.

Ketefian, G., and M. Z. Jacobson (2009), A mass, energy, vorticity, and potential enstrophy conserving boundary treatment scheme for the shallow water equations, *J. Comp. Phys.*, *228*, 1–32, doi:10.1016/j.jcp.2008.08.009.

Kettle, A. J., et al. (1999), A global database of sea surface dimethylsulfide (DMS) measurements and a procedure to predict sea surface DMS as a function of latitude, longitude, and month, *Global Biogeochem. Cycles*, *13*, 399–444.

Klimont, Z., D. G. Streets, S. Gupta, J. Cofala, L. Fu, and Y. Ichikawa (2002), Anthropogenic emissions of non-methane volatile organic compounds (NMVOC) in China, *Atmos. Environ.*, *36*, 1309–1322.

Lamb, B., H. Westberg, G. Allwind, L. Bamesberger, and A. Guenther (1987), Measurement of biogenic sulfur emissions from soils and vegetation: Application of dynamic enclosure methods with Natusch filter and GC/FPD analysis, *J. Atmos. Chem.*, *5*, 469–491.

Liao, H., W.-T. Chen, and J. H. Seinfeld (2006), Role of climate change in global predictions of future tropospheric ozone and aerosols, *J. Geophys. Res.*, *111*, D12304, doi:10.1029/2005JD006852.

Logan, J. A. (1999a), An analysis of ozonesonde data for the troposphere: Recommendations for testing 3-D models, and development of a gridded climatology for tropospheric ozone, *J. Geophys. Res.*, *104*, 16,115–16,149.

Logan, J. A. (1999b), An analysis of ozonesonde data for the lower stratosphere: Recommendations for testing models, *J. Geophys. Res.*, *104*, 16,151–16,170.

Low, T. B., and R. List (1982), Collision, coalescence and breakup of raindrops: part I. Experimentally established coalescence efficiencies and fragment size distributions in breakup, *J. Atmos. Sci.*, *39*, 1591–1606.

Marticorena, B., G. Bergametti, B. Aumont, Y. Callot, C. N'Doume, and M. Legrand (1997), Modeling the atmospheric dust cycle: 2. Simulation of Saharan dust sources, *J. Geophys. Res.*, *102*, 4387–4404.

Martin, R. V., B. Sauvage, I. Folkins, C. E. Sioris, C. Boone, P. Bernath, and J. Ziemke (2007), Space-based constraints on the production of nitric oxide by lightning, *J. Geophys. Res.*, *112*, D09309, doi:10.1029/2006JD007831.

Miller, P. D. (1985), Maize pollen: Collection and enzymology, in *Maize for Biological Research. A Special Publication of the Plant Molecular Biology Association*, chap. 45, edited by W. F. Sheridan, pp. 279–282, Charlottesville, Va.

Mouli, P. C., S. V. Mohan, and S. J. Reddy (2005), Assessment of microbial (bacteria) concentrations of ambient air at semi-arid urban region: Influence of meteorological factors, *Appl. Ecol. Environ. Res.*, *3*, 139–149.

Murazaki, K., and P. Hess (2006), How does climate change contribute to surface ozone change over the United States, *J. Geophys. Res.*, *111*, D05301, doi:10.1029/2005JD005873.

Nakicenovic, N., et al. (2000), *Emissions Scenarios: A Special Report of the Intergovernmental Panel on Climate Change*, Cambridge Univ. Press, New York.

National Institute for Public Health and the Environment (RIVM) (2001), *The IMAGE 2.2 Implementation of the SRES Scenarios: A Comprehensive Analysis of Emissions, Climate Change and Impacts in the 21st Century* [CD-ROM], RIVM Publ. 481508018, Bilthoven, Netherlands.

Ogden, E. C., and J. V. Hayes (1969), Diurnal patterns of pollen emission in Ambrosia, Phleum, Zea, and Ricinus, *Am. J. Bot.*, 56, 16–21.

Olivier, J. G. J., A. F. Bouwman, C. W. M. Van der Maas, J. J. M. Berdowski, C. Veldt, J. P. J. Bloos, A. J. H. Visschedijk, P. Y. J. Zandveld, and J. L. Haverlag (1996), Description of EDGAR Version 2.0: A set of global emission inventories of greenhouse gases and ozone-depleting substances for all anthropogenic and most natural sources on a per country basis on $1° \times 1°$ grid, National Institute of Public Health and the Environment, *RIVM Rep. 771060002/TNO-MEP Rep. R96/119*.

Pasken, R., and J. A. Pietrowicz (2005), Using dispersion and mesoscale meteorological models to forecast pollen concentrations, *Atmos. Environ.*, 39, 7689–7701.

Posfai, M., J. Li, J. R. Anderson, and P. R. Buseck (2003), Aerosol bacteria over the Southern Ocean during ACE-1, *Atmos. Res.*, 66, 231–240.

Pickering, K. E., Y. Wang, W.-K. Tao, C. Price, and J.-F. Muller (1998), Vertical distributions of lightning NOx for use in regional and global chemical transport models, *J. Geophys. Res.*, 103, 31,303–31,216.

Price, C., and D. Rind (1992), A simple lightning parameterization for calculating global lightning distributions, *J. Geophys. Res.*, 97, 9919–9933.

Price, C., J. Penner, and M. Prather (1997), NO_x from lightning: 1. Global distribution based on lightning physics, *J. Geophys. Res.*, 102, 5929–5941.

Petzold, A., A. Dopelheuer, C. A. Brock, and F. Schroder (1999), In situ observations and model calculations of black carbon emission by aircraft at cruise altitude, *J. Geophys. Res.*, 104, 22,171–22,181.

Pruppacher, H. R., and J. D. Klett (1997), *Microphysics of Clouds and Precipitation*, 2nd rev. and enl. ed., Kluwer Academic Publishers, Dordrecht.

Reponen, T. (1995), Aerodynamic diameters and respiratory deposition estimates of viable fungal particles in mold problem dwellings, *Aerosol Sci. Technol.*, 22, 11–23.

Ridley, B. A., K. E. Pickering, and J. E. Dye (2005), Comments on the parameterization of lightning-produced NO in global chemistry-transport models, *Atmos. Environ.*, 39, 6184–6187.

Rutledge, S. A., E. R. Williams, and T. D. Keenan (1992), The down under Doppler and electricity experiment (DUNEE): Overview and preliminary results, *Bull. Am Meteorol. Soc.*, 73, 3–16.

Sakiyan, N., and O. Inceoglu (2003), Atmospheric concentrations of Cladosporium Link and Alternaria Nees spores in Ankara and the effects of meteorological factors, *Turk. J. Bot.*, 27, 77–81.

Sanderson, M. G., C. D. Jones, W. J. Collins, C. E. Johnson, and R. G. Derwent (2003), Effects of climate change on isoprene emissions and surface ozone levels, *Geophys. Res. Lett.*, 30(18), 1936, doi:10.1029/2003GL017642.

Schumann, U., and H. Huntrieser (2007), The global lightning-induced nitrogen oxides source, *Atmos. Chem. Phys. Discuss.*, 7, 2623–2818.

Shaffer, B. T., and B. Lighthart (1994), Survey of airborne bacteria at four diverse locations in Oregon: Urban, rural, forest, and coastal, available at http://www.isb.vt.edu/BRARG/BRASYM94/SHAFFER.HTM.

Shaw, R. H., D. P. Ward, and D. E. Aylor (1979), Frequency of occurrence of fast gusts of wind inside a corn canopy, *J. Appl. Meteorol.*, 18, 167–171.

Sillman, S., and P. J. Samson (1995), Impact of temperature on oxidant photochemistry in urban, polluted rural, and remote environments, *J. Geophys. Res.*, 100, 11,497–11,508.

Smith, M. H., and N. M. Harrison (1998), The sea spray generation function, *J. Aerosol Sci.*, 29, Suppl. 1, S189–S190.

Steiner, A. L., S. Tonse, R. C. Cohen, A. H. Goldstein, and R. A. Harley (2006), Influence of future climate and emissions on regional air quality in California, *J. Geophys. Res.*, 111, D18303, doi:10.1029/2005JD006935.

Stevenson, D. S., C. E. Johnson, W. J. Collins, R. G. Derwent, and J. M. Edwards (2000), Future estimates of tropospheric ozone radiative forcing and methane turnover - the impact of climate change, *Geophys. Res. Lett.*, 27, 2073–2076.

Stevenson, D., R. Doherty, M. Sanderson, C. Johnson, B. Collins, and D. Derwent (2005), Impacts of climate change and variability on tropospheric ozone and its precursors, *Faraday Discuss.*, 130, 1–17.

Streets, D. G., et al. (2003a), An inventory of gaseous and primary aerosol emissions in Asia in the year 2000, *J. Geophys. Res.*, 108(D21), 8809, doi:10.1029/2002JD003093.

Streets, D. G., K. F. Yarber, J.-H. Woo, and G. R. Carmichael (2003b), Biomass burning in Asia: Annual and seasonal estimates and atmospheric emissions, *Global Biogeochem. Cycles*, 17(4), 1099, doi:10.1029/2003GB002040.

Streets, D. G., T. C. Bond, T. Lee, and C. Jang (2004), On the future of carbonaceous aerosol emissions, *J. Geophys. Res.*, 109, D24212, doi:10.1029/2004JD004902.

Sutkus, D. J., S. L. Baughcum, and D. P. DuBois (2001), Scheduled Civil Aircraft Emission Inventories for 1999: Database Development and Analysis, *NASA/CR-2001-211216*, available at http://gltrs.grc.nasa.gov/reports/2001/CR-2001-211216.pdf.

Tie, X., R. Zhang, G. Brasseur, and W. Lei (2002), Global NO_x production by lightning, *J. Atmos. Chem.*, 43, 61–74.

Thompson, A. M., R. W. Stewart, M. A. Owens, and J. A. Herwehe (1989), Sensitivity of tropospheric oxidants to global chemical and climate change, *Atmos. Environ.*, 23, 519–532.

Unger, N., D. T. Shindell, D. M. Koch, M. Ammann, J. Cofala, and D. G. Streets (2006), Influences of man-made emissions and climate changes on tropospheric ozone, methane, and sulfate at 2030 from a broad range of possible futures, *J. Geophys. Res.*, 111, D12313, doi:10.1029/2005JD006518.

United States Environmental Protection Agency (USEPA) (2006), Clearinghouse for Inventories and Emission Factors, available at http://www.epa.gov/ttn/chief/.

United States Geological Survey (USGS) (2008), MODIS/Aqua Leaf-Area Index, available at http://edcdaac.usgs.gov/modis/myd15a2v4.asp.

United States Geological Survey (USGS), U. Nebraska, Lincoln, and European Commission's Joint Research Center (1999), 1-km resolution global landcover characteristics data base, derived from Advanced Very High Resolution Radiometer (AVHRR) data from the period April 1992 to March 1993.

Wang, C., and R. G. Prinn (2000), On the roles of deep convective clouds in tropospheric chemistry, *J. Geophys. Res.*, 105, 22,269–22,297.

Wang, Y., D. J. Jacob, and J. A. Logan (1998), Global simulation of tropospheric O_3-NO_x-hydrocarbon chemistry: 1. Model formulation, *J. Geophys. Res.*, 103, 10,713–10,725.

Wanninkhof, R. (1992), Relationship between wind speed and gas exchange over the ocean, *J. Geophys. Res.*, 97, 7373–7382.

Warneck, P. (1999), *Chemistry of the Natural Atmosphere*, Elsevier, New York.

Woo, J.-H., et al. (2003), Contribution of biomass and biofuel emissions to trace gas distributions in Asia during the TRACE-P experiment, *J. Geophys. Res.*, 108(D21), 8812, doi:10.1029/2002JD003200.

Zeng, G., and J. A. Pyle (2003), Changes in tropospheric ozone between 2000 and 2100 modeled in a chemistry-climate model, *Geophys. Res. Lett.*, 30(7), 1392, doi:10.1029/2002GL016708.

Zhang, Y., C. H. Bischof, R. C. Easter, and P.-T. Wu (1998), Sensitivity analysis of a mixed phase chemical mechanism using automatic differentiation, *J. Geophys. Res.*, 103, 18,953–18,979.

———————————

M. Z. Jacobson, Department of Civil and Environmental Engineering, Stanford University, Yang and Yamazaki Environment and Energy Building, Room 397, Stanford, CA 94305-4020, USA. (jacobson@stanford.edu)

D. G. Streets, Decision and Information Sciences Division, Argonne National Laboratory, DIS/900, 9700 South Cass Avenue, Argonne, IL 60439, USA. (dstreets@anl.gov)